Geophysical Journal International

Geophys. J. Int. (2015) **203,** 1–21 doi: 10.1093/gji/ggv251

GJI Marine geosciences and applied geophysics

Distribution of melt along the East Pacific Rise from 9°30′ to 10°N from an amplitude variation with angle of incidence (AVA) technique

Milena Marjanović,[1,*] Hélène Carton,[1] Suzanne M. Carbotte,[1] Mladen R. Nedimović,[1,2] John C. Mutter[1] and J. Pablo Canales[3]

[1] *Department of Marine Geology and Geophysics, Lamont-Doherty Earth Observatory, Palisades, NY* 10964-8000*, USA. E-mail: marjanovic@ipgp.fr*

[2] *Department of Earth Sciences, Dalhousie University, Halifax, Nova Scotia* B3H 4R2*, Canada*

[3] *Department of Geology and Geophysics, Woods Hole Oceanographic Institution, Woods Hole, MA* 02543-1050*, USA*

Accepted 2015 June 9. Received 2015 June 8; in original form 2014 October 25

SUMMARY

We examine along-axis variations in melt content of the axial magma lens (AML) beneath the fast-spreading East Pacific Rise (EPR) using an amplitude variation with angle of incidence (AVA) crossplotting method applied to multichannel seismic data acquired in 2008. The AVA crossplotting method, which has been developed for and, so far, applied for hydrocarbon prospection in sediments, is for the first time applied to a hardrock environment. We focus our analysis on 2-D data collected along the EPR axis from 9°29.8′N to 9°58.4′N, a region which encompasses the sites of two well-documented submarine volcanic eruptions (1991–1992 and 2005–2006). AVA crossplotting is performed for a ∼53 km length of the EPR spanning nine individual AML segments (ranging in length from ∼3.2 to 8.5 km) previously identified from the geometry of the AML and disruptions in continuity. Our detailed analyses conducted at 62.5 m interval show that within most of the analysed segments melt content varies at spatial scales much smaller (a few hundred of metres) than the length of the fine-scale AML segments, suggesting high heterogeneity in melt concentration. At the time of our survey, about 2 yr after the eruption, our results indicate that the three AML segments that directly underlie the 2005–2006 lava flow are on average mostly molten. However, detailed analysis at finer-scale intervals for these three segments reveals AML pockets (from >62.5 to 812.5 m long) with a low melt fraction. The longest such mushy section is centred beneath the main eruption site at ∼9°50.4′N, possibly reflecting a region of primary melt drainage during the 2005–2006 event. The complex geometry of fluid flow pathways within the crust above the AML and the different response times of fluid flow and venting to eruption and magma reservoir replenishment may contribute to the poor spatial correlation between incidence of hydrothermal vents and presence of highly molten AML. The presented results are an important step forward in our ability to resolve small-scale characteristics of the AML and recommend the AVA crossplotting as a tool for examining mid-ocean ridge magma-systems elsewhere.

Key words: Mid-ocean ridge processes; Submarine tectonics and volcanism; Crustal structure; Physics of magma and magma bodies.

1 INTRODUCTION

As two plates separate, solid mantle ascends and decompresses resulting in molten, buoyant rock (or magma), which then moves upwards, towards the surface. A large portion of the upwelling melt may pond within the uppermost mantle at the base of the newly formed oceanic crust (Toomey *et al.* 1990, 2007). From this subcrustal accumulation, melt further ascends, and at fast to intermediate spreading centres collects into intracrustal magma sills or axial magma lenses (AMLs; Detrick *et al.* 1987; Sinton & Detrick 1992; and reference therein). These lenses are suggested to act as the main magma source reservoirs for the formation of the upper and some of the lower oceanic crust and play a central role in mid-ocean ridge (MOR) crest hydrothermal circulation and volcanic activity.

Given the importance of the AML, its physical properties have been the subject of many geophysical studies over the past ∼30 yr (e.g. Detrick *et al.* 1987, 1993; Harding *et al.* 1989; Kent *et al.* 1990, 1993a,b; Vera *et al.* 1990; Caress *et al.* 1992; Hussenoeder *et al.*

[*] Now at: Equipe de Géosciences Marines, Institut de Physique du Globe de Paris, 1 rue Jussieu, F-75238 Paris Cedex 05, France.

1996; Collier & Singh 1997, 1998; Singh *et al.* 1998, 1999). Results from these studies showed that on the East Pacific Rise (EPR) at 9–10°N, the AML is present at 1–2 km below the seafloor, and is, on average 0.5–1.2 km wide (Kent *et al.* 1993a), and ∼30–100 m thick (Collier & Singh 1997; Singh *et al.* 1998; Xu *et al.* 2014). Recently, it has been suggested that the AML is partitioned into fine-scale lens segments, extending ∼5–15 km in the along-axis direction (Carbotte *et al.* 2013). The reversed polarity of the AML reflection compared to that of the seafloor reflection (e.g. Vera *et al.* 1990) and the presence of a wide-angle shadow zone (Orcutt *et al.* 1975; Detrick *et al.* 1987) were used as first-order proxies to argue that the material within the sill is possibly molten. Shear wave properties of the AML have been used to infer both qualitative and quantitative estimates of the melt content within the AML (Singh *et al.* 1998; Canales *et al.* 2006; Xu *et al.* 2014), however the amount of melt available within the AML at different locations where good seismic control is available remains poorly constrained.

One of the best-studied portions of the MOR system is the EPR at 9°50′N (Fig. 1). It is characterized by intense volcanic, hydrothermal and biological activity (e.g. Haymon *et al.* 1991, 1993; Shank *et al.* 1998; Von Damm 2004; Tolstoy *et al.* 2006, 2008; Soule *et al.* 2007), and is also the site where a reflection from the AML was first identified in multichannel seismic (MCS) data (Herron *et al.* 1978, 1980). Unambiguous images and improved knowledge of the AML in this area were obtained from a two-ship seismic survey conducted in 1985, which provided seismic section with higher signal-to-noise ratio (Detrick *et al.* 1987; Mutter *et al.* 1988; Vera *et al.* 1990; Kent *et al.* 1993a). In 2008, a multisource, multistreamer MCS survey (cruise MGL0812) was carried out in the region spanning the ridge axis from 9°38′ to 9°57′N (Mutter *et al.* 2009, 2010, 2014).

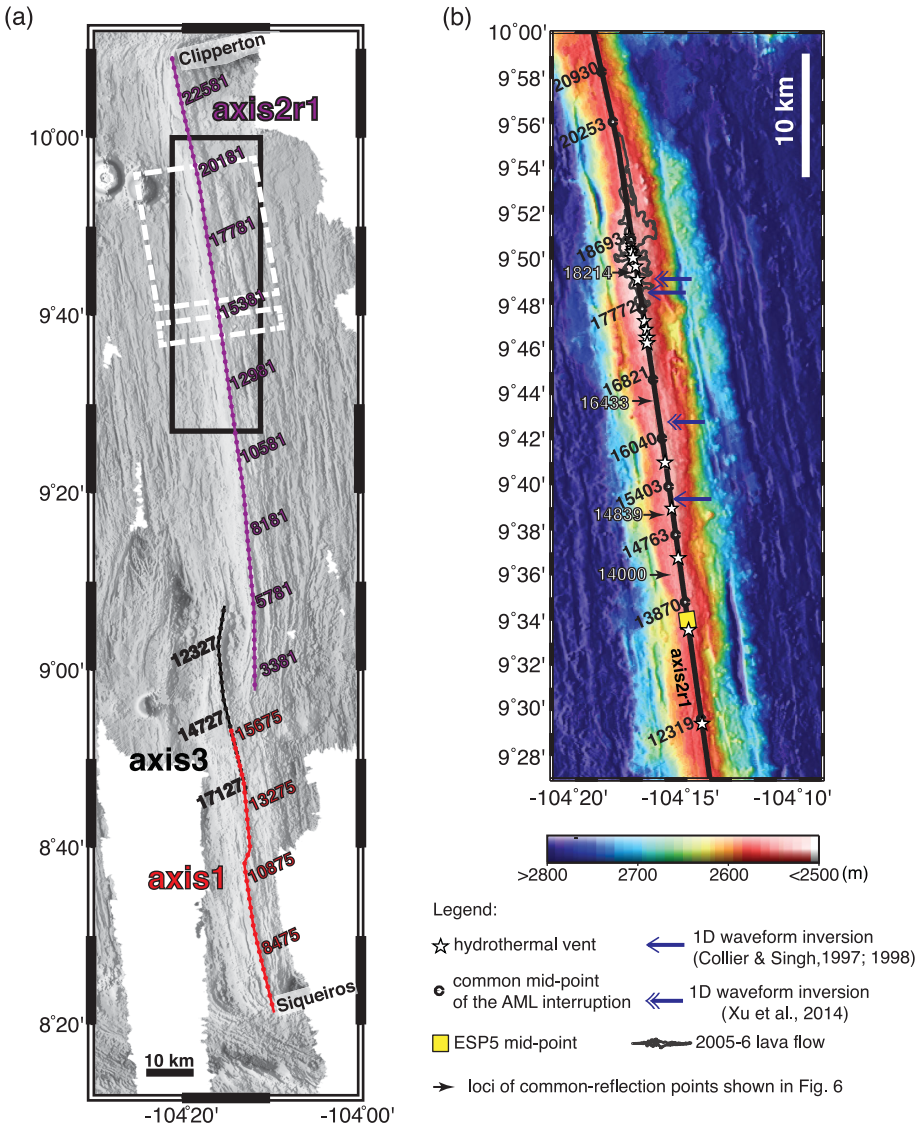

Figure 1. Survey area (a) track lines of along-axis MCS data from expedition MGL0812 used in this study (sail lines axis1, axis2r1 and axis3). These lines run closest to the innermost axial zone. Dots are placed at every 300 common mid-point (CMP) interval, that is every 1875 m along each track. Background is a grey-scale bathymetric image of the EM120 multibeam echo-sounder data collected during the same survey and gridded at 50 m. Locations of 3-D seismic volumes obtained from cross-axis acquisition are shown with dashed white rectangles. Area of close-up in (b) is indicated in black rectangle. (b) Location map for the AVA study conducted between 9°29.8′ and 9°58.4′N. The location of seismic line axis2r1/hydrophone-cable 2 used for the analysis is shown in black. Circles indicate locations of small disruptions in the axial magma lens as mapped by Carbotte *et al.* (2013). Bathymetry the same as in panel (a). Outline of the 2005–2006 lava flow is from Fundis *et al.* (2010). See legend for other symbols.

In addition to the main ridge-perpendicular survey acquired for 3-D imaging of crustal structure (Canales *et al.* 2012a,b; Aghaei *et al.* 2014; Han *et al.* 2014), an along-axis swath survey (Carbotte *et al.* 2013; Marjanović *et al.* 2014; Xu *et al.* 2014) was conducted (Fig. 1a). The along-axis survey was designed to facilitate examination of spatial variations in the internal properties of the AML, as variations in seafloor topography of the overlying crust are minimal in this direction, resulting in relatively simpler wave propagation and therefore allowing for more accurate data analysis.

In this study, using a single along-axis seismic line closest to the axial summit trough – AST (Fornari *et al.* 1998a, 2004) along the crest of the EPR (axis2r1; Mutter *et al.* 2009; Fig. 1b), we seek to determine the distribution of melt beneath the ridge axis. As a tool for data analysis we use a standard petroleum exploration amplitude variation with angle of incidence (AVA) technique based on the crossplotting of seismic attributes (Castagna *et al.* 1998; Ross 2000; Pelletier 2008; Foster *et al.* 2010). In the literature, amplitude variation with offset (AVO) crossplotting is interchangeably used with AVA to describe the same technique (e.g. Foster *et al.* 2010; and references therein). However, the two terms, AVA and AVO, can be considered equivalent only for a shallow, horizontal and planar reflector, for which angle of incidence of a given trace can be approximated by its source–receiver offset (Shang *et al.* 1993). In all other cases conversion from offset to angle of incidence has to be applied and data re-organized from common mid point (CMP) gathers to common reflection point (CRP) gathers (Resnick 1993; Shang *et al.* 1993). Failing to do the above may result in amplitude-smearing and inaccurate amplitudes (Shang *et al.* 1993). Here, we apply the conversion from offset to angle of incidence and thus use the AVA acronym.

We perform AVA analysis over a ∼53 km long section of the ridge between 9°29.8′N and 9°58.4′N (Fig. 1). Within this region our analysis reveals variations in the melt content of adjoining lens segments with five out of nine AML segments characterized as mostly to highly molten. Fine-scale analysis done at 62.5 m interval shows that melt content varies at spatial scales much smaller (a few 100s of metres) than the length of the fine-scale AML segments (3.2–8.5 km), arguing for limited magma mixing within a thin lens. Within the three AML segments underlying the lava flow erupted during a documented volcanic eruption in 2005–2006 (Tolstoy *et al.* 2006; Cowen *et al.* 2007; Soule *et al.* 2007) and where intense hydrothermal activity is observed (e.g. Haymon *et al.* 1991; Von Damm 2004; Fornari *et al.* 2012), our results indicate that active high-temperature vents are located above both molten and partially molten portions of the AML. Furthermore, we estimate that within the portion of the eruption area where the most voluminous flow lobes were emplaced (9°47.9–9°52′N), the volume of melt available in the AML pre-eruption was likely insufficient to account for the lava volume emplaced onto the seafloor during the last eruption event. This supports the view emerging from several recent studies that the eruption may have been sourced from deeper magma reservoirs in the mid to lower crust.

2 BACKGROUND

2.1 Geological setting

The portion of the fast-spreading (full spreading rate of 108–109 mm yr^{-1}; Carbotte & Macdonald 1992) northern EPR that was sampled by the 2008 along-axis MCS survey extends from the Siqueiros Transform Fault at 8°20′N to the Clipperton Transform Fault at 10°10′N. Nested scales of tectonic segmentation are identified within this region, with the finest-scale segmentation defined by small jogs (<0.5 km) or bends (<5°) in the axial eruptive fissure zone (Haymon *et al.* 1991; Macdonald *et al.* 1992; Fornari *et al.* 1998b; White *et al.* 2006). Beneath the innermost axial zone, the AML is imaged along ∼85 per cent of the length of the ridge, and appears as a generally bright reflection event located on average ∼1.6 km below the seafloor (Carbotte *et al.* 2013). Through visual inspection of 3-D across-axis data and swath along-axis data, along with analysis of instantaneous attributes calculated for the along-axis lines, disruptions of the AML marked by steps in two-way travel time (TWTT), edge diffractions in stack sections and/or regions of two AML reflections that overlap in depth are identified (Carbotte *et al.* 2013; Marjanović 2013). The locations of these disruptions partition the AML into fine-scale (∼5–15 km long) segments, which roughly coincide with the fine-scale tectonic segmentation of the ridge as observed in the morphology of the axial zone (Carbotte *et al.* 2013; Marjanović 2013).

The EPR region around 9°50′N experienced two well-documented volcanic eruptions in 1991–1992 (Haymon *et al.* 1993; Rubin *et al.* 1994; Gregg *et al.* 1996) and 2005–2006 (Tolstoy *et al.* 2006; Cowen *et al.* 2007; Soule *et al.* 2007; Goss *et al.* 2010), which both occurred as multiple discrete episodes over the course of several months (Rubin *et al.* 1994, 2012). The estimated volume of erupted lavas in 2005–2006 was ∼4–5 times larger than that erupted in 1991–1992 (Soule *et al.* 2007). The 2005–2006 lava flow extended between ∼9°45.6′ and 9°55.7′N and gave rise to multiple flow lobes fed through either pre-existing or new lava channels (Soule *et al.* 2005; Fundis *et al.* 2010). The largest flow lobe extended to distances of 2–3 km off-axis in the 9°51′N area (Fig. 1b). Results of geochemical analyses (including major and trace element analyses and Sr, Nd and Pb isotopic ratios) conducted on basaltic glasses formed during the 2005–2006 eruption, along with earlier analyses conducted on samples from the 1991–1992 eruption event, indicate that the AML was refilled with more evolved residual liquids in the repose time between the two eruptions (Goss *et al.* 2010). Goss *et al.* (2010) suggest that these residual liquids originated from the underlying mush zone and that no injection of large volumes of fresh magma from the mantle occurred prior to the 2005–2006 event. In contrast Moore *et al.* (2014) argued, on the basis of zoning of plagioclase crystals that focused primitive magma replenishment from the deep part of the lower crust or uppermost mantle (which took place only 6 weeks prior to the eruption) played a predominant role in triggering the eruption event.

The EPR 9°50′N area is also characterized by abundant hydrothermal venting (Haymon *et al.* 1991; Von Damm 2000; Fig. 1b). High-temperature (>300 °C), focused hydrothermal discharge forming sulfide chimneys is primarily concentrated between 9°46′ and 9°51′N where the axial summit trough hosts two distinct vent clusters (centred at 9°47′ and 9°50′N), with individual vent spacing on the order of 50 to 200 m within each cluster (e.g. Fornari *et al.* 2004). With respect to the first visual survey conducted in 1989 (Haymon *et al.* 1991), several high-temperature vents have become extinct (Tubeworm Pillar no longer active in 2003; M and Q following the 2005–2006 eruption) and new vent sites have appeared (e.g. Hobbit Hole, Crab Spa, Tamtown; Fornari *et al.* 2012). Moreover, at the active vent sites, variations in vent fluid temperature, chemistry and biological colonization (Shank *et al.* 1998; Cowen *et al.* 2007) have been recorded through the magmatic cycle (e.g. Sohn *et al.* 1998, 1999; Fornari *et al.* 1998b; Von Damm 2004; Scheirer *et al.* 2006).

2.2 Seismic methods used to estimate AML melt content

Several approaches have been developed for qualitative or quantitative assessment of the AML melt content from MCS data. This, in turn, allows for examination of the relationship between melt fraction, eruption history and hydrothermal venting. The occurrence of a *P*-to-*S* converted phase reflected off the AML and converted back to *P* at the seafloor (hereinafter $P_{\mathrm{AML}}S$) has been used to infer melt-to-mush variations and to study spatial relations with hydrothermal venting at fast (e.g. Singh *et al.* 1998) and intermediate (Canales *et al.* 2006) spreading centres. Calculated reflection coefficient variations as a function of offset or horizontal slowness (e.g. Singh *et al.* 1998) indicate that in the case of a melt-rich AML, the $P_{\mathrm{AML}}S$ amplitude is expected to be significantly larger at offsets $>\sim$1.5 km than in the case of a melt-poor AML. Concurrently, for a melt-rich AML, the reflected *P*-wave signal ($P_{\mathrm{AML}}P$) should be weak at mid-offsets and a change in polarity of the event is expected (e.g. Vera *et al.* 1990; Hussenoeder *et al.* 1996).

Waveform forward modelling (Hussenoeder *et al.* 1996) and waveform inversion techniques (Collier & Singh 1997, 1998; Singh *et al.* 1998; Canales *et al.* 2006; Xu *et al.* 2014) have provided estimates of the melt content within the AML, by determining *P*- and *S*-wave velocities and comparing the resulting values with experimental observations (e.g. Murase & McBirney 1973) and/or predictions such as from an effective medium theory (e.g. Hashin & Shtrikman 1963). Full waveform inversion is computationally expensive and requires a good prior knowledge of the long wavelengths of the velocity model. Except for the recent work of Arnulf *et al.* (2014), who examined the physical properties of the Axial Volcano magma body in 2-D, published applications of elastic full waveform inversion to oceanic spreading centre AML reflections have been limited thus far to 1-D analysis of data from point locations (Collier & Singh 1997, 1998; Singh *et al.* 1998, 1999; Canales *et al.* 2006; Xu *et al.* 2014). Most recently, a 1-D waveform inversion study was performed using data from our along-axis EPR 2008 survey at two contrasting locations: 9°42.8′ and 9°49.1′N (Xu *et al.* 2014; locations in Fig. 1b). Whereas at the southern location results indicate the presence of a high melt fraction (>70 per cent), at the northern location they suggest the presence of low melt fraction (<40 per cent).

3 DATA ANALYSIS

3.1 *A* (intercept) versus *B* (slope) crossplotting

The amplitude variations of a seismic reflection event as a function of the angle of incidence at the corresponding interface are entirely described by the Knott-Zoeppritz equations (Zoeppritz 1919; for complete derivation see Yilmaz 2001). Owing to their complexity these reflection coefficient equations have seen little direct use (Hilterman 2001; Yilmaz 2001), and linearizing approximations are routinely implemented (see Appendix A).

Shuey's (1985) approximation of the *P*-wave reflection coefficient equation involves seismic attributes *A*—reflection-coefficient intercept or normal-incidence reflection coefficient, and *B*—the reflection-coefficient gradient or reflection-coefficient slope. *A* and *B* values are calculated from velocity-reduced gathers, that is, normal move out (NMO)-corrected CMP gathers (e.g. Ross 2000) or pre-stack time migrated CRP gathers (e.g. Resnick 1993). The determination of *A* and *B* is usually done through least squares fitting of a straight line and sometimes by more statistically robust approaches (e.g. Walden 1991). Another approach uses angle stacks (e.g. Foster *et al.* 2010), with *A* extracted from a near-angle stack (incidence angle up to ∼20°), and *B* calculated as the difference between the same near-angle stack and the mid-angle stack (usually calculated from a range of incidence angles of 20°–30°) divided by the square of the sin of the incidence angle at mid-angles. Angle stacks are used in this study.

Combining seismic attributes *A* (intercept) and *B* (slope) in a crossplot diagram has proven an effective way for discriminating among AVA responses (e.g. Castagna & Swan 1997). The two main elements of a typical *A* versus *B* crossplot diagram (Fig. 2) for oil-industry applications are a background trend characterizing 'non-pay' background and anomaly characterizing possible hydrocarbon-bearing regions or anomalous lithology (e.g. Castagna *et al.* 1998; Ross 2000; Foster *et al.* 2010). In practice, the background trend is estimated from either seismic or well data across the interface between reservoir sedimentary rock and seal rock in a region devoid of hydrocarbons. In the case of small elastic perturbations, the background trend follows a line in the crossplot with its slope defined by $1-8\left(\frac{V_{s1}+V_{s2}}{V_{p1}+V_{p2}}\right)^2$, called the 'fluid line'. For $\langle V_p\rangle/\langle V_s\rangle = 2$ the slope of the fluid line is -1 and its equation is thus $B = -A$. For $\langle V_p\rangle/\langle V_s\rangle \neq 2$, Foster *et al.* (2010) show that there is a good agreement between predicted background trends and AVA behaviour modelled from well logs. When pores of the same reservoir rock are filled with hydrocarbons, *A* and *B* values plot as a deviation from the background trend, that is anomaly (Fig. 2).

3.2 *A* (intercept) versus *B* (slope) crossplotting interpretation scheme for MOR studies

While the *A* versus *B* (or AVA) crossplotting technique is common practice within the commercial sector, existing crossplot interpretation schemes (e.g. Foster *et al.* 2010) do not apply directly to the MOR environment. The lithology and structural setting at MORs are very different from those of typical hydrocarbon environments, where variations in AVA response are related to fluid replacement within the pores of a sedimentary rock. Here, the source of the AML reflection event is a thin lens of magma (mixture of molten rock, crystals and dissolved gases) that ponds at the base of the sheeted dyke layer and caps a broader zone of hot rock and distributed partial melt in the lower crust (e.g. Sinton & Detrick 1992; Fig. 3). It is the variations in melt fraction and the connectivity of melt and crystals within the magma body that give rise to variations in AVA response. Furthermore, on the ridge flanks, there is no evidence from modern MCS data for a reflection signal related to the boundary between sheeted dykes and lower crustal gabbro (i.e. layer 2/layer 3 boundary), that is, the stratigraphic level occupied by the AML at the ridge axis (Fig. 3). As a result, a background trend analogous to that defined for a potential hydrocarbon reservoir rock cannot be defined in the MOR environment.

Another significant difference is the strength of the velocity contrast at the interface of interest: as small elastic perturbation assumption is not appropriate to describe the AVA behaviour of the AML, across which large *P*-wave velocity contrasts of $\Delta V_p \approx 1700$–$2600\ \mathrm{m\ s^{-1}}$ may occur. Foster *et al.* (1997, 2010) provided the basis for the interpretation of the crossplots in the case of arbitrarily large seismic velocity contrasts but assuming no contrast in density. In this case, Foster *et al.* (2010) showed that *B* can be expressed as a function of *A* as follows:

$$B = \left(1-8\gamma^2\right)A - 4\gamma\Delta\gamma\left(1-\Delta\gamma\right) + \left(1-2\gamma\right)\mathrm{O}\left(A^2\right) \qquad (1)$$

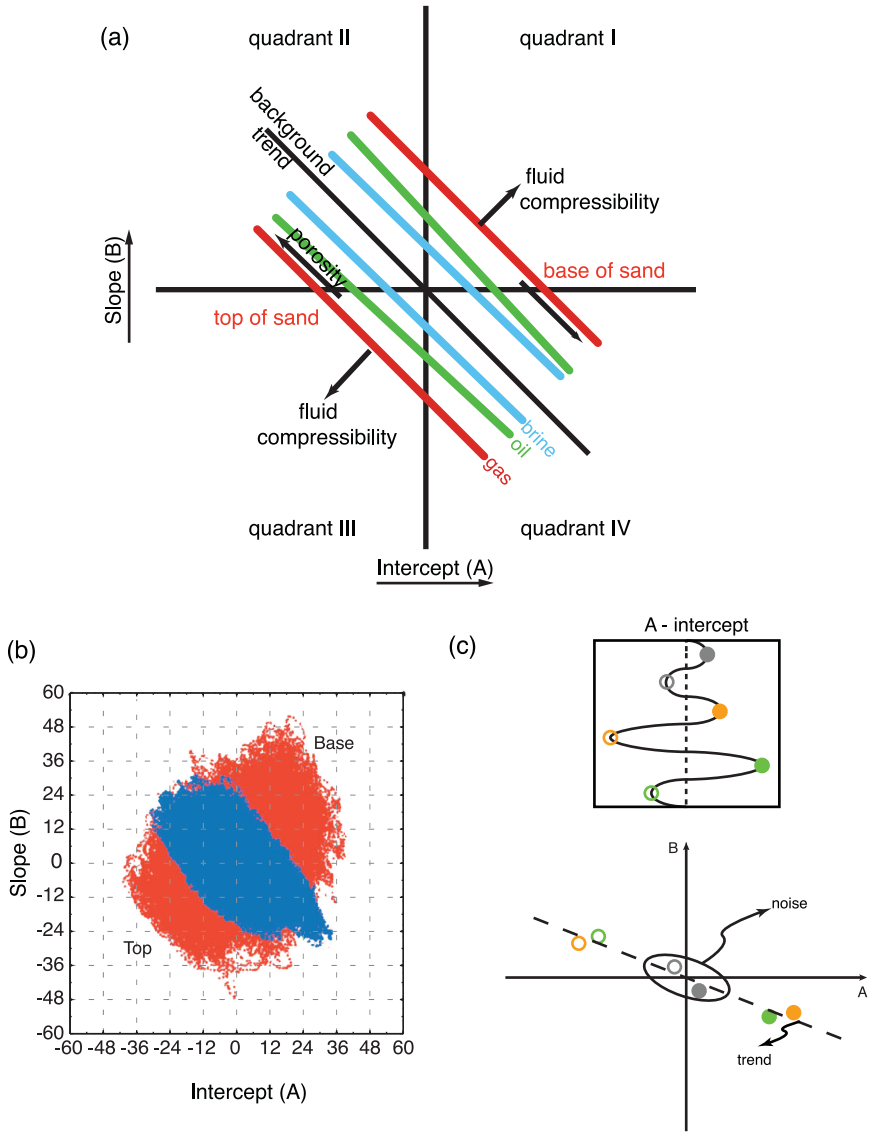

Figure 2. Background on AVA crossplotting. (a) Schematic oil-industry intercept versus slope crossplot modified from Foster *et al.* (2010). AVA anomaly trend responses are shown for brine (blue), oil (green), and gas (red) for the top of reservoir sands (below the background trend line) and the base of reservoir sands (above the background trend line). Arrows indicate effects of increases in fluid compressibility and reservoir porosity. (b) Example taken from Foster *et al.* (2010), showing respective domains for the background trend (obtained for the region devoid of hydrocarbons) in blue and for the hydrocarbon anomaly (reservoir interval) in red for a 3-D data set. The background trend is defined from the cloud of blue dots, as the direction of the major axis of the smallest ellipse that encompasses all the points. (c) Example of a near-angle waveform with negative (open circles) and positive (filled circles) peaks highlighted, and location of the corresponding (A, B) pairs in the crossplot diagram: for each common reflection point (CRP) location; (A, B) pairs are calculated at all TWTTs of near-angle amplitude extrema encountered within the analysis window.

with: $\gamma = \frac{V_s}{V_p} = \frac{V_{s1}+V_{s2}}{V_{p1}+V_{p2}}$ and (neglecting second-order terms): $\Delta\gamma = \frac{\Delta V_s}{\langle V_s\rangle} - \frac{\Delta V_p}{\langle V_p\rangle} = \frac{2(V_{s2}V_{p1}-V_{s1}V_{p2})}{(V_{p1}+V_{p2})^2}$.

For a *P*-wave velocity contrast at AML interface $\Delta V_p \approx 1700$–2600 m s^{-1}, the corresponding density contrast $\Delta\rho \approx 100$ kg m^{-3} (Murase & McBirney 1973) can be considered negligible, since the absolute value of *P*-wave velocity and density difference ratio ($\Delta V_p/\Delta\rho$) for the AML case ($\sim$17–26 m^4 s^{-1} kg) is comparable to that of a sandstone/shale interface ($\Delta V_p \approx 500$–1300 m s^{-1}; $\Delta\rho \approx 32$ kg m^{-3} leads to $\Delta V_p/\Delta\rho$ of $\sim$16–40 m^4 s^{-1} kg).

On the basis of eq. (1), and because of the impossibility to define a background trend from regions devoid of AML, we develop an interpretation template based on a comparison between theoretical trend lines computed for different $\langle V_p\rangle/\langle V_s\rangle$ ratios (Fig. 4). Similar to Castagna *et al.* (1998), we define a series of linear trends going through the origin of the crossplot, corresponding to a different, constant value of $\langle V_p\rangle/\langle V_s\rangle$. Each of the ratios is obtained from available estimates of *P*-wave velocities for the AML (V_{p2}) and its roof (V_{p1}) (Vera *et al.* 1990; Kent *et al.* 1993a; Singh *et al.* 1998), *S*-wave velocity of the AML roof taken as $V_{s1} = V_{p1}/\sqrt{3}$, and available estimates of V_{s2} that encompass melt to mush cases (Singh *et al.* 1998; Xu *et al.* 2014). The $\langle V_p\rangle/\langle V_s\rangle$ values tested here range from 1.55 to 2.3 at an increment of 0.15 and from 2.3 to 2.5. An AML with a high melt fraction is characterized by larger decreases in V_p and V_s across the interface than an AML with a low melt fraction, assuming that the roof velocities are unchanged. This results in a higher $\langle V_p\rangle/\langle V_s\rangle$ and thus a trend line closer to horizontal for an AML with a high-liquid fraction, whereas a lower $\langle V_p\rangle/\langle V_s\rangle$

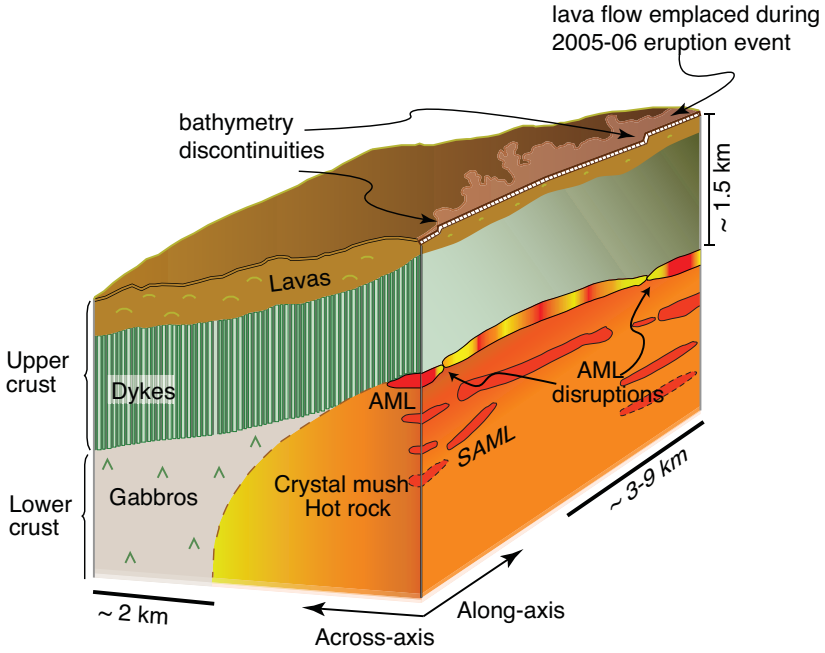

Figure 3. Structure and lithology at fast to intermediate spreading centres. An AML caps the mush zone at the ridge axis within which subaxial magma lenses have been recently imaged (Marjanović *et al.* 2014). The contact between sheeted dykes and gabbros on the ridge flanks does not produce an imageable reflection. Color within the AML represents along-axis variations in melt content with yellow/red indicating low/high melt contents respectively. Variations in melt content within the SAML are unknown.

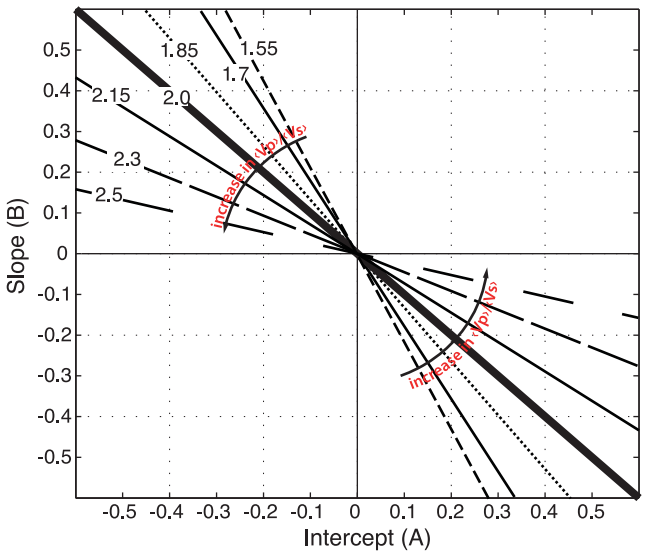

Figure 4. *A* versus *B* crossplot template showing calculated trend lines for different constant $\langle V_p \rangle / \langle V_s \rangle$ ratios (labeled). Melt-rich segments (higher $\langle V_p \rangle / \langle V_s \rangle$) are expected to show a counter-clockwise rotation of the trend line compared to melt-poor segments.

and more vertical trend line characterize an AML with a low-liquid fraction (Table 1). Fig. 4 illustrates this counterclockwise rotation of the calculated trend as melt content in AML increases. However, the calculated trends are non-unique as different combinations of V_{p1}, V_{s1}, V_{p2}, V_{s2} can produce the same $\langle V_p \rangle / \langle V_s \rangle$.

In addition, it is important to examine the interpretability of AVA results in the thin layer case. The thin bed (Widess 1973; Sheriff 1975; Kallweit & Wood 1982) configuration is relevant for AML studies, since most results for the northern EPR 9°30′-10°N

Table 1. Examples of trends calculated using plausible V_p and V_s velocities for AML interface (first column represents an example of partially molten case and second column highly molten case).

Velocity \ $\langle V_p \rangle / \langle V_s \rangle$	2	2.2
V_{p1} (km s^{-1})	6.32	6.32
V_{p2} (km s^{-1})	4.55	2.95
V_{s1} (km s^{-1})	3.65	3.65
V_{s2} (km s^{-1})	1.75	0.53

area (apart from those of Hussenoeder *et al.* 1996) suggest that the thickness of the AML is ≤50 m (Kent *et al.* 1993a; Collier & Singh 1997; Xu *et al.* 2014). The effect of a thin bed on AVA results has been studied by, among others, Juhlin & Young (1993), Lin & Phair (1993), Bakke & Ursin (1998), and Liu & Schmitt (2003). These studies have demonstrated that the AVA response of a thin layer can show significant departure from the AVA response of a simple interface. For increasing incidence angles, there is a decrease in the delay time $2d \cos \theta / V_p$ (where d is layer thickness) between the reflection off the bottom and the reflection off the top of the layer. Thus, a gradually more oblique incidence angle is equivalent to a gradually thinner bed at vertical incidence (Juhlin & Young 1993; Liu & Schmitt 2003). This translates into a decrease in the normalized AVA response of thin layers for $d \leq \lambda/4$ (in our case $\lambda/4 = \sim$30–45 m, calculated using a dominant frequency ∼20–30 Hz, and assuming *P*-wave velocity within the sill of 3–4.5 km s^{-1} from Vera *et al.* 1990). Hussenoeder *et al.* (1996) computed amplitude versus slowness curves for a thin magma lens (testing $d = 5$, 20, 40, 60, 80 and 100 m) and obtained a family of curves that follow similar amplitude fall-off patterns, but with rates (as well

as, of course, vertical-incidence amplitudes) dependent on AML thickness. These results suggest that variable tuning related to variations in AML thickness may contribute to seismic amplitudes recorded at all angles along our profile. The effect of a thin bed on intercept versus slope crossplotting results has not been addressed extensively in prior studies. Ross (2000) showed that when the reservoir thickness is decreased to either 50 per cent or 75 per cent of the tuning thickness (maximum constructive interference for layer thickness $d = \sim\lambda/4$; Widess 1973), the background trend is defined equally well, but the vector that connects a background trend point to its corresponding anomaly point resulting from pore fluid substitution becomes more parallel to the A-axis, instead of being roughly oriented at 45° from *A* and *B* axes. Ross (2000) concluded that the presence of a thin bed complicates the interpretation of the crossplots. In the absence of needed AML thickness constraints along the EPR axis, we interpret differences in AVA behaviour between AML sections in the framework of a constant-thickness AML, that is, assuming these differences are the effect of variations in melt fraction only.

3.3 Seismic data

3.3.1 EPR data selection for AVA analysis

The acquisition layout for the along-axis swath survey used two flip-flopping source arrays spaced 75 m apart and four 6-km long streamers spaced 150 m apart (Mutter *et al.* 2009). Each source was a tuned broadband 18-airgun array totaling 3300 cu. in. and towed at a depth of 7.5 m. Each sail line was processed separately with 2-D geometry assigned, which results in a nominal CMP fold of 78. The feathering angle was ≤7° along most of profile axis2r1 and remained moderate (≤11°) throughout the survey. Fig. 1a shows a composite along-axis profile that runs closest to the morphological axis, corresponding to portions of sail lines axis1 and axis3 south of the 9°03′N overlapping spreading centre, and axis2r1 north of it. The main changes in orientation of the morphological axis, such as in the 9°56′N area, were accommodated as bends in the seismic line during acquisition. In this study, we use the recordings by one of the innermost streamers of shots fired by both sources. Within the areas in which the AML was imaged in 3-D (Carton *et al.* 2014; Han *et al.* 2014) the chosen along-axis line (here axis2r1) generally samples the central shallow crest of the AML; this is however not true for the region centred around 9°56′N where there is a bend in the ridge axis and at 9°44′N where the chosen line crosses the middle of an offset/discontinuity between two lens segments. To select locations for the application of the focused AVA analysis presented here, we performed partial-offset stacking of $P_{\mathrm{AML}}S$ reflection on the entire first-order segment extending from 8°20′N to 10°10′N (Figs 1a and 5a). The corresponding data processing sequence is given in Marjanović *et al.* (2014). The resulting images show the presence of a distinct (though variable in strength) $P_{\mathrm{AML}}S$ phase between 9°37′ and 10°02′N, whereas elsewhere, the $P_{\mathrm{AML}}S$ signal is either very weak (e.g. from 9°30′ to 9°32′N) or absent. On the basis of earlier studies that have used $P_{\mathrm{AML}}S$ as an indicator of the presence of melt-rich AML (e.g. Singh *et al.* 1998; Canales *et al.* 2006), variable melt content along the ridge axis is anticipated. The bathymetry of the EPR axis south of 9°10′N exhibits significant short-wavelength roughness (e.g. White *et al.* 2006) that may cause lower signal-to-noise ratio and may contribute to lower-amplitude AML reflections; this, in turn, makes this region less suitable for the AVA analysis. On the basis of partial-offset stacking results, we decided to apply the AVA crossplotting method on the portion of the EPR extending for ∼53 km between 9°29.8′N and 9°58.4′N (Fig. 5b–d).

3.3.2 Data processing for AVA analysis

Data preparation prior to the extraction of seismic attributes for AVA analysis follows standard oil-industry procedures (Castagna 1993; Yilmaz 2001) with care taken to preserve relative amplitudes (Resnick 1993). Processing steps include trace editing, filtering and noise suppression, and spherical divergence correction (Table 2). No correction was made for array directivity. After binning into 78 offset bins, each 75 m wide, the CMP data were pre-stack time migrated, generating CRP gather output. A 1-D velocity function based on ESP5 results (Vera *et al.* 1990; see Fig. 1b for location of this study) was used as a starting velocity function for migration velocity analysis. The velocity field for pre-stack time migration (PSTM) was obtained by performing velocity analyses at every ∼400 CRP (about every 2.5 km). After PSTM, a Radon filter (e.g. Foster & Mosher 1992; Sacchi & Ulrych 1995) was applied to remove undesired noise: the data were transformed into the τ-p domain where a mute was picked to attenuate arrivals showing a move-out different from that of the primary reflection (here, the AML event). Since the AVA analysis is based on attributes extracted from stacked sections, it is important that the event of interest is flattened at all source–receiver offsets included in the partial-angle stacks. We therefore conducted a second pass of velocity analyses on CRP supergathers obtained by vertically stacking 24 adjacent CRPs located at approximately 625 m intervals along the profile. This improved velocity field was used for the final residual moveout (RMO) correction (Fig. 6). The final rms velocity model was also used to convert the data from source–receiver offset/ TWTT domain to angle of incidence/TWTT (e.g. Fig. 6). The CRP-sorted data were then stacked (Fig. 7).

The intercept versus slope crossplotting method requires formation of a near-angle stack and mid-angle stack. Since the minimum incidence angle for the EPR seismic data set varies between ∼2.9° and ∼4° along the profile, we chose 5° as the minimum angle for the near-angle stack for consistency between segments. Shuey's approximation is valid for angles ≤30° (Appendix A), therefore we used 30° as the maximum angle for computation of the mid-angle stack. In agreement with previous work (e.g. Foster *et al.* 2010), we chose 20° as the boundary between near- and mid-angle stacks. In Fig. 6 we show selected CRP gathers that display flattened AML event for the range of angles used in the AVA analysis. The resulting near- and mid-angle stacks are shown in Figs 7(b) and (c), respectively. A summary of the processing sequence is given in Table 2.

3.4 *A* (intercept) versus *B* (slope) crossplotting from 9°29.8′N to 9°58.4′N

In this study, we use the ABAVO module within the GeoCraft© crossplotting software developed by ConocoPhillips, with earlier applications shown in Foster *et al.* (2010). To form an *A* (intercept) versus *B* (slope) crossplot, a window along CRP and TWTT axes needs to be defined, within which the analysis is performed. In a first step, we use the length of the nine AML segments centred at 9°32.4′, 9°36.2′, 9°38.7′, 9°41′, 9°43.3′, 9°46.3′, 9°49.3′, 9°53.6′ and 9°57.4′N (Figs 1 and 5; Table 3; Carbotte *et al.* 2013), to define the along-axis extents of the windows for AVA analysis, resulting in nine crossplots (Fig. 8). These segments are defined based on

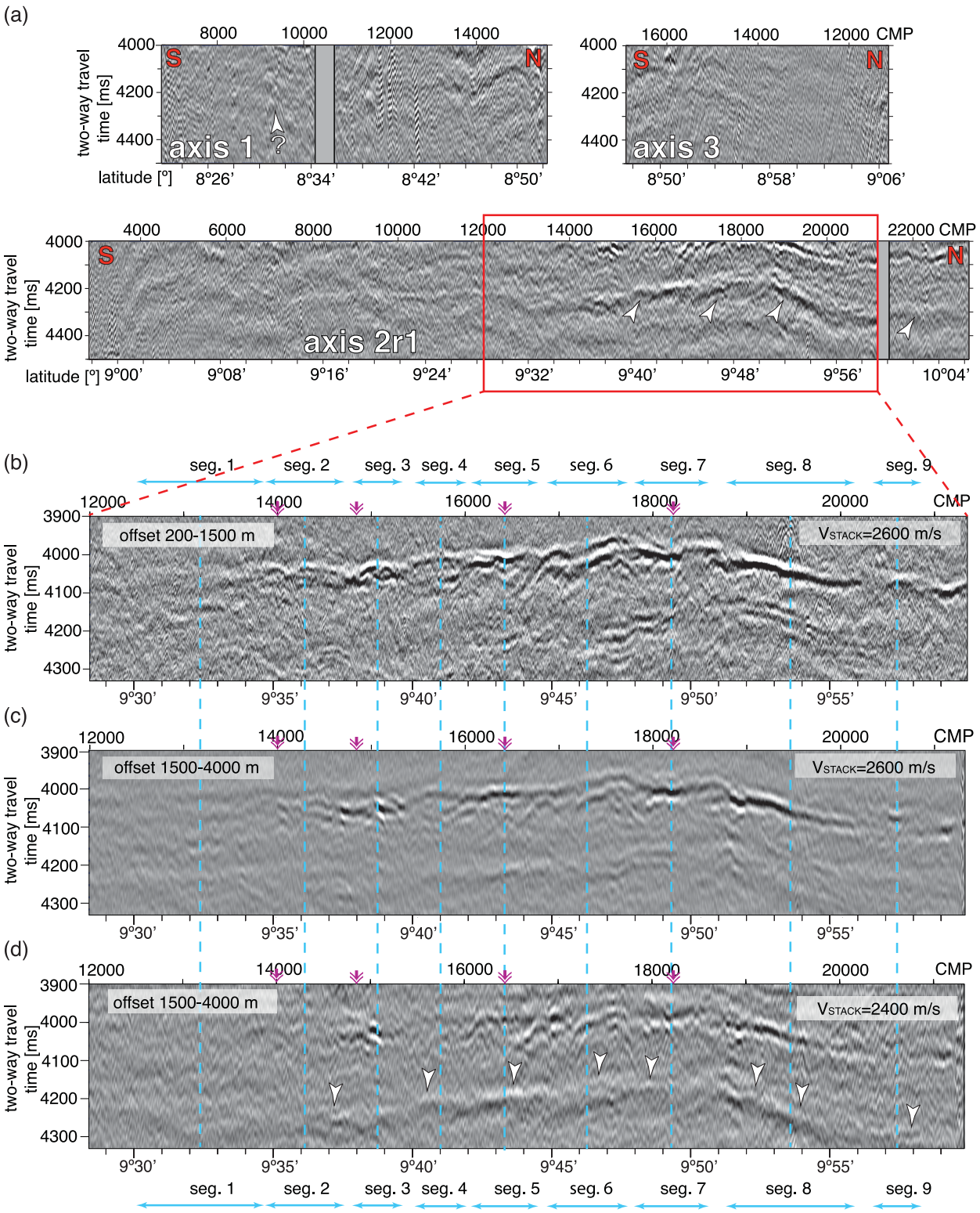

Figure 5. Partial offset stacking. (a) Mid-offset (1500–4000 m) stack of lines axis1, axis3 and axis 2r1 spanning from 8°22′ to 10°06′N (Fig. 1a) and computed using a stacking velocity of $V = 2400$ m s^{-1}, appropriate for the *P*-to-*S* converted wave reflected off the AML ($P_{\mathrm{AML}}S$ phase). Where present, the $P_{\mathrm{AML}}S$ arrival is indicated by white arrowheads; its TWTT is generally ∼200 ms below the *P*-wave reflection event at the AML ($P_{\mathrm{AML}}P$ phase). Red rectangle indicates close-up region between 9°28.5′ and 9°59.5′N shown in panels (b), (c) and (d). Grey rectangles indicate gaps in the data. (b) Near source-receiver offset (200–1500 m) stack generated with a stacking velocity $V = 2600$ m s^{-1} optimal for the $P_{\mathrm{AML}}P$ event. (c) Mid-offset (1500–4000 m) stack computed using the same $V = 2600$ m s^{-1} stacking velocity; (d) $P_{\mathrm{AML}}S$ stack enlarged from panel (a). White arrowheads indicate $P_{\mathrm{AML}}S$ event, and blue lines mark centres of AML segments which extent is shown with filled black circles in Fig. 1(b). Segments are numbered 1 to 9. Double-headed purple arrows indicate approximate locations of the 4 CRP gathers shown in Fig. 6. For comparison purposes, panels (b), (c) and (d) are shown with the same gain. Positive amplitudes are displayed in black and negative amplitudes in white.

Table 2. Processing sequence.

Processing scheme	Comments
Trace editing	AXIS 2R1 navigation lines 3 and 4
2-D geometry definition	–
Band-pass filtering	Butterworh single, zero phase filter: 10/18–100/72 [(F1 dB/Octave 1)-(F2 dB/Octave 2)]
Noise suppress	Spike and noise burst edit; trace edits applied
Spherical divergence correction	Gain correction $g(t) = t * v(t)$.
Kirchhoff pre-stack time migration	CMP sorting prior to migration data were grouped into 78 bins (bin spacing 75 m) required by the KTMIG module. Data are migrated using modified ESP5 velocity function hung from the seafloor
Radon filtering	Parabolic τ-p transform for p values between −200 and 2000 (ms); trace muting
Accurate/residual normal-moveout correction (NMO)	Apply inverse RMO using migration velocities combining 24 consecutive CMP gathers into super-CMP gathers; semblance analysis performed to flatten AMC event at every 100 super CMP gather; band-pass Ormsby, single filter: 4–12.5–40–50
Angle-gathers	Angles are calculated using 1-D approximation to the input velocity field at each CMP; near-angle gather for 5–20° (maximum average offset ∼1800 m depending on the AMC depth and interval velocity); far-angle gather for 20–30° (∼1800–2800 m)
Stacking	Near-angle (intercept A) stack 5–20° and far-angle (slope B) stack 20–30°

the geometry of the AML and the presence of disruptions in its along-axis continuity (Fig. 9 shows examples of the *A* versus *B* relationship in the crossplot domain for four AML disruptions present within the eruption area). Segments vary in length between ∼3.2 and 8.5 km (Table 3). Along the TWTT axis sampled at 4 ms, the window length is defined for each segment individually (Fig. 7a; Table 3): here we chose a window length of 120 ms for all segments, centred on the first break of the AML event at the middle CRP of each segment, except for segment 8 for which the window width is set to 160 ms TWTT to ensure that the AML event is fully captured.

In an *A* versus *B* crossplot diagram a cloud of points is obtained, each point corresponding to one (A, B) pair, with *A* and *B* values determined from near-angle and mid-angle stacked trace amplitudes within the analysis window (Figs 2b and c). At each CRP location, *A* and *B* pairs are obtained for all amplitude extrema (including noise) found within the desired time interval of the analysis window (Figs 2c and 7a). Thus, each peak/trough combination on the stacked near- and mid-angle trace generates two points in the crossplot diagram that may be roughly symmetrical with respect to the origin (Fig. 2c). Low-amplitude noise present within the analysis window will give rise to low As and Bs in absolute value, whereas reflection events will give rise to As and Bs that plot away from the origin. This attribute extraction based on amplitudes within the analysis window around the AML TWTT provides As and Bs that are proportional to but not necessarily equal to the theoretical As and Bs of the reflection coefficient eq. (A.2). This is because the calculation of the true vertical-incidence reflection coefficient (theoretical attribute A) at the AML typically makes use of recorded amplitudes at the seafloor and seafloor multiple, in addition to the AML amplitude (e.g. Vera *et al.* 1990), whereas here only the AML amplitude is used. Through a normalization process within the crossplotting software, extracted As and Bs are scaled to a range between 0 and 0.5 that is reminiscent of what one would expect for the theoretical values. Thus, slopes in the crossplot diagrams as well as relative variations between crossplot diagrams can be readily interpreted, but not exact As and Bs. For each cloud of points, we calculated a best-fit trend as the direction of the major axis of the smallest ellipse enclosing all data points. The crossplots for all nine AML segments are shown in Fig. 8 with further information given in Table 3. Crossplotting is performed on a trace-by-trace basis, hence for any given length of segment analysed each CRP location will yield the same suite of (A, B) pairs. The best-fit trend line for the anomaly may, of course, vary for different lengths of the analysis window along the CRP axis, as a result of averaging.

The above segment-scale analysis implicitly assumes that melt is to first order uniformly distributed within individual fine-scale AML segments (Fig. 10a). To test this hypothesis we applied the same crossplotting method at a finer spatial scale, including the AML discontinuity regions, for completeness (Figs 10b and c). To this end, we chose an analysis window length of 10 CRPs (∼62.5 m). With this setup, the correlation coefficient of the trend, which is a measure of the quality of the linear fit to the cloud of points, is generally larger in absolute value than 0.8 in the individual crossplots, thus indicating well-constrained $\langle V_p \rangle / \langle V_s \rangle$; only a few regions show less well-constrained $\langle V_p \rangle / \langle V_s \rangle$ (absolute value correlation coefficient 0.5–0.8; Fig. 10).

The horizontal resolution of unmigrated data is given by the diametre of the first Fresnel zone. Using the expression of the normal-incidence Fresnel diametre as a function of depth to the interface and dominant wavelength λ (see for instance Lindsey 1989), we obtain a Fresnel diametre at the AML of ∼0.8 to ∼1.0 km using the Berkhout criterion (λ/8) and ∼1.1 to ∼1.4 km using the Sheriff criterion (λ/4), assuming a dominant frequency of 20 to 30 Hz at the AML. The Fresnel diametre in the direction perpendicular to the profile is unchanged and equal to its pre-migration value. The 2-D along-axis data used in our crossplotting analysis are pre-stack time migrated, hence the Fresnel diametre in along-axis direction is collapsed to its migrated size, and our fine-scale analysis at ∼62.5 m intervals is consistent with this. In areas where the reflecting body is narrower than the diametre of the first Fresnel zone, the diffractions from the edges interfere with the primary reflection signal (e.g. Knapp 1991). In some sections of our study area an AML width of ∼500 m has been inferred (Kent *et al.* 1990, 1993a; Carton *et al.* 2014), while elsewhere the width of the AML is on the scale of the Fresnel diametre. We acknowledge these limitations in resolution, which could be mitigated in further studies by conducting AVA analysis on the 3-D data set.

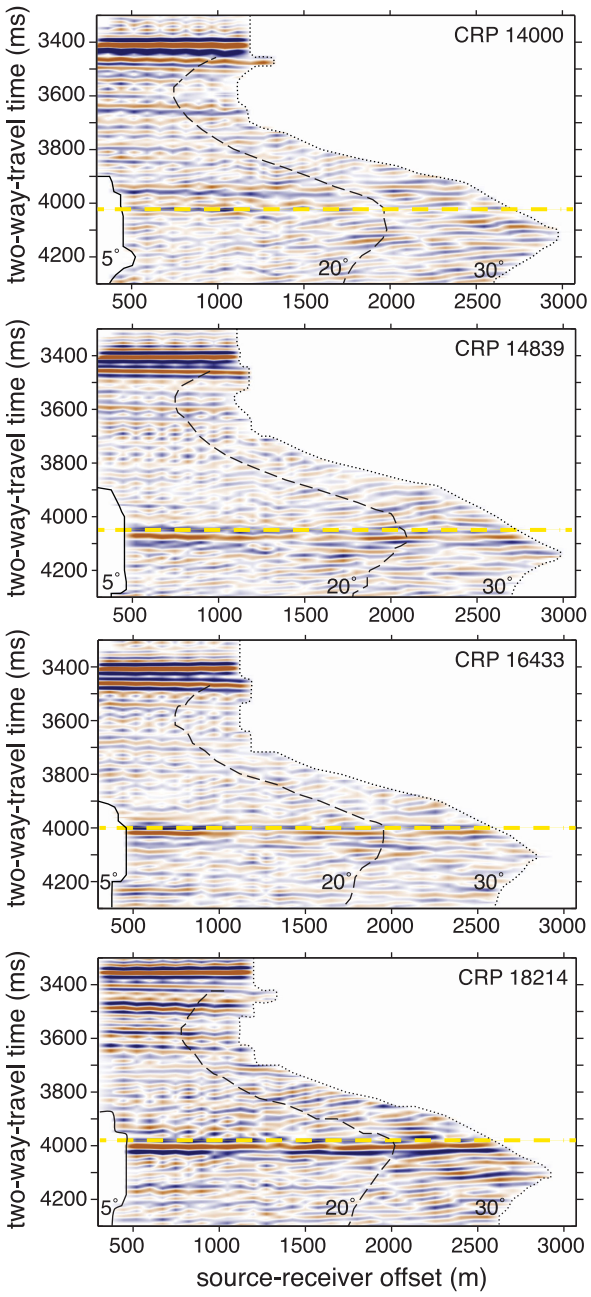

Figure 6. Selected CRP gathers after pre-stack migration and residual moveout correction (RMO) to flatten the AML event. Positive amplitudes are displayed in red and negative amplitudes in blue. Gathers provide examples of partially molten AML (CRP 14 000), mostly molten (CRP 14 839) and highly molten AML (CRP 16 433 and 18 214) as determined from the AVA results. Solid (5°), dashed (20°) and dotted (30°) black lines represent boundaries of incidence angle domains superimposed on the time-offset gather. The conversion from offset to angle of incidence is performed using the final migration velocity function. Horizontal yellow dashed line is to indicate flatness of the event across offsets. See Table 2 for detailed processing sequence.

4 RESULTS AND INTERPRETATION OF CROSSPLOTS

4.1 Crossplot characteristics

The resulting crossplots (Figs 8 and 9) show scattered anomalies that are clearly centred at the origin, that is they do not plot along shifted lines as in the schematic diagram of Fig. 2(a). Such observation is uncommon but not unique to the MOR environment (Fig. 2b). The second term in eq. (1) accounts for most of this shift and for it to be equal to zero either $\Delta\gamma = 1$ or $\Delta\gamma = 0$. Since the latter condition describes the 'special' case of background trend or fluid line, for the anomaly to be centred on the origin $\Delta\gamma$ has to be equal to one, that is $2(V_{s2}V_{p1} - V_{s1}V_{p2}) = (V_{p1} + V_{p2})^2$. It has been speculated that $\Delta\gamma = 1$ could be obtained for a special case of velocity gradient layer above the interface of interest (Foster, private communication, 2011). The presence of a gradient zone marking the transition between the solid roof of the AML and the AML itself has been inferred at locations along both the Northern and Southern EPR (Vera *et al.* 1990; Singh *et al.* 1999). Further work required to fully examine this possible explanation is outside the scope of this paper.

Another evident characteristic of the crossplots formed from the analysed EPR data is that they do not suggest the existence of distinct families of trends, but rather gradational range of AVA responses. For interpretation purposes and by comparison with the calculated template (see Section 3.2; Fig. 4) and results from previous studies we define three categories: (1) we call partially molten (or solid to mushy) all regions with $\langle V_p\rangle/\langle V_s\rangle \leq 2.06$ (as this is the maximum value of the trend for which $P_{AML}S$ is not observed; Fig. 5); (2) we call mostly molten all regions with $2.06 < \langle V_p\rangle/\langle V_s\rangle \leq 2.15$ and (3) we call highly molten all regions for which $\langle V_p\rangle/\langle V_s\rangle > 2.15$ (as a very prominent $P_{AML}S$ signal is observed above this trend value; Fig. 5d).

Several additional characteristics can be noted. The range of As and Bs over which the clouds of points extend is less when the AML is inferred to be partially molten: $0.1 \leq \max|A| \leq 0.25$ and $0.13 \leq \max|B| \leq 0.22$, than when it is inferred to be mostly to highly molten: $0.25 \leq \max|A| \leq 0.53$ and $0.22 \leq \max|B| \leq 0.44$ (Table 3). This result for the intercept A is reasonable, because higher absolute values of the vertical-incidence reflection coefficient (theoretical attribute A) are expected when the melt fraction is high. For a low melt fraction maximum absolute values of attribute A may be higher for a thin sill than for a simple interface, owing to the tuning effect. Where the AML is inferred to be mostly to highly molten, more scattering is observed not only along the trend but also across the trend, sometimes quite distinctly (segment 8; Fig. 8). Overall, best-fit trends for both compact and large ellipses display linear correlation coefficients between A and B to define the trend line generally >0.8 in absolute value (all segments except segments 1, 2 and 3; Fig. 10a; Table 3) and are thus considered to be well defined. Because (A, B) pairs associated with noise tend to gather near the origin, this low level noise is assumed to have a minimal effect on the trends defined from the reflection signal in the data.

4.2 Results and interpretation at different scales

4.2.1 Segment-scale analysis

From the series of nine crossplots obtained along the length of our study area, we identify five segments – segment 3 (centred at 9°38.7′N), segment 5 (centred at 9°43.3′N), segment 6 (centred at 9°46.3′N), segment 7 (centred at 9°49.3′N) and segment 8 (centred at 9°53.6′N) – that are characterized by $\langle V_p\rangle/\langle V_s\rangle > 2.06$ as derived from the best-fit trends (Fig. 8; Table 3). According to the proposed classification, these AML segments are mostly- to highly molten (Fig. 10a). Among them, segment 5 has the highest $\langle V_p\rangle/\langle V_s\rangle$ ratio (2.19), suggesting a liquid composition within this section. Trends

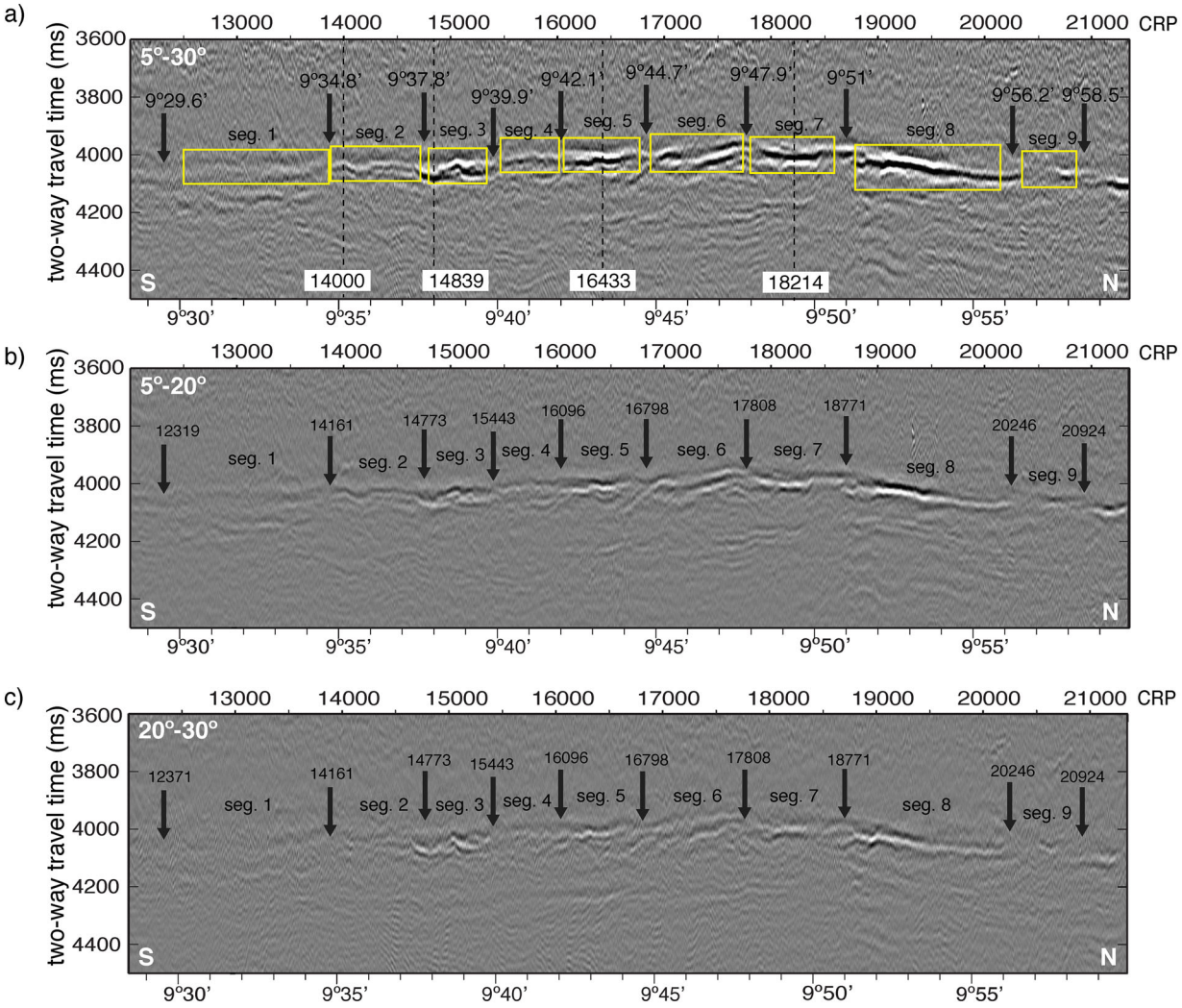

Figure 7. Angle stacks: (a) stack of pre-stack migrated data for the full range of incidence angles at the AML used in this study (5° to 30°), equivalent to offsets of ∼350 to 2650–2800 m. Dashed lines indicate locations of the example CRP gathers shown in Fig. 6. Yellow rectangles show analysis windows used to perform AVA crossplotting for each of the nine AML segments defined in the area (Figs 1b and 4b): segment 1 centred at 9°32.4′, segment 2 at 9°36.2′, segment 3 centred at 9°38.7′, segment 4 centred at 9°41′, segment 5 at 9°43.3′, segment 6 centred at 9°46.3′, segment 7 at 9°49.3′, segment 8 centred at 9°53.6′ and segment 9 at 9°57.4′. (b) Stack of pre-stack migrated data for 5° to 20° incidence angle at the AML interface (near-angle, corresponding to offsets of ∼350 to 1900–2100 m). (c) Stack of pre-stack migrated data for 20° to 30° incidence angle at the AML interface (mid-angles, corresponding to offsets of ∼1900–2100 to 2650–2800 m). Black arrows in all panels indicate interruptions in the AML reflection with corresponding latitude labeled in (a) and CRP numbers labeled in (b) and (c).

Table 3. Statistics of the crossplots presented in Figs 8 and 9.

	CRP	∼Length (m)	TWTT window (ms)	# *A*, *B* pairs	Corr coef.	$\langle V_p \rangle / \langle V_s \rangle$	max |A|	max |B|
Segment 1	12 500–13 860	8500	3980–4100	19 590	−0.77	1.9	0.106	0.174
Segment 2	13 880–14 720	5250	3970–4090	11 616	−0.78	2.06	0.15	0.187
Segment 3	14 800–15 340	3375	3975–4095	7024	−0.8	2.15	0.271	0.222
Segment 4	15 470–16 020	3440	3940–4060	7888	−0.82	2.04	0.173	0.179
Segment 5	16 060–16 770	4440	3940–4060	9732	−0.9	2.18	0.324	0.246
Segment 6	16 870–17 740	5440	3940–4060	11 646	−0.92	2.13	0.271	0.254
Segment 7	17 800–18 590	4875	3940–4060	10 258	−0.92	2.13	0.351	0.32
Segment 8	18 790–20 150	8500	3965–4125	18 242	−0.93	2.14	0.532	0.441
Segment 9	20 350–20 860	3190	3990–4110	7106	−0.86	1.99	0.251	0.218
Discont. 9°44.7′	16 773–16 870	606	3940–4060	1236	−0.87	1.93	0.171	0.205
Discont. 9°47.9′	17 748–17 796	300	3940–4060	678	−0.92	1.9	0.123	0.133
Discont. 9°51′	18 597–18 790	1206	3940–4060	2496	−0.86	2.11	0.253	0.217
Discont. 9°56.2′	20 156–20 350	1213	3990–4110	3068	−0.85	1.93	0.178	0.137

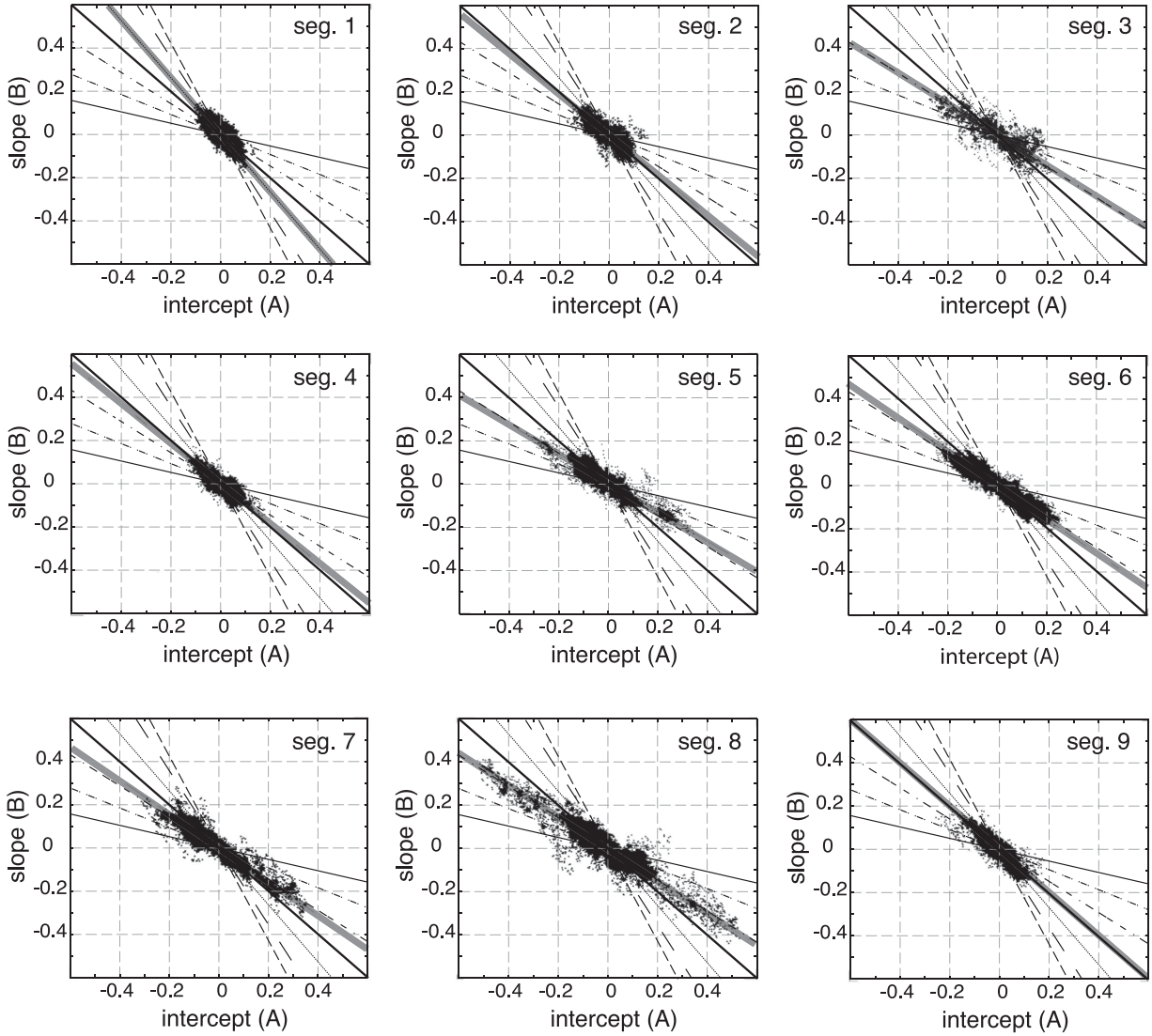

Figure 8. *A* versus *B* crossplots obtained for the nine fourth-order AML segments within the analysis windows outlined in Fig. 7(a). Each CRP gather gives rise to several (A, B) pairs, of which only one is generated by the negative excursion of the AML waveform at vertical incidence (others are from positive excursions, and noise above and below the AML). The best-fit trend is plotted with a thick solid grey line. Calculated trend lines from the template are shown as in Fig. 4.

for segments 1, 2, 4 and 9 correspond to $\langle V_p \rangle / \langle V_s \rangle \leq 2.06$ (Fig. 8) and we interpret these AML segments to be partially molten (Fig. 10a).

4.2.2 *Fine-scale analysis*

We conduct fine-scale *A* versus *B* crossplotting for the entire region extending between 9°29.8′ and 9°58.4′N (Figs 10b and c).

Eruption area (segments 6, 7 and 8). Whereas the segment-scale trends suggest that the three AML segments located below the seafloor that extend across the 2005–2006 eruption are mostly molten, analysis conducted at 10 CRPs (∼62.5 m) interval indicates the presence of smaller scale variations in melt concentration from partially to highly molten (Fig. 10b). The width of the zones of homogeneous behaviour varies from ∼62.5 m (one cell length) to 1375 m. Along most of the length of segment 6, $\langle V_p \rangle / \langle V_s \rangle$ is >2.06 (mostly to highly molten), except between 9°45.5′ and 9°46′N and at the bounding discontinuities. Within segment 7 several regions with $\langle V_p \rangle / \langle V_s \rangle \leq 2.06$ (partially molten) are identified, the longest one being centred at ∼9°50.4′N (∼800 m long) and within the southern portion of this segment. Segment 8 shows predominantly $\langle V_p \rangle / \langle V_s \rangle > 2.06$ (mostly to highly molten), with only a few short (up to ∼300 m long) partially molten regions. This segment also displays a ∼1375 m long highly molten region, with $\langle V_p \rangle / \langle V_s \rangle \geq 2.3$, which represents the highest $\langle V_p \rangle / \langle V_s \rangle$ value encountered in this analysis.

Between ∼9°52′ and 9°52.9′N the largest values of *A* and *B* are observed within a zone ranging from mostly to highly molten (Fig. 10b), and are responsible for the increased scatter in the crossplot of segment 8 (Fig. 8). This suggests a local enhancement of seismic reflectivity not primarily related to melt fraction. Interestingly, geochemistry study of samples from lavas erupted in 2005–2006 (Goss *et al.* 2010) indicate that lavas emplaced within the same region are slightly enriched in iron and titanium. Laboratory studies (Karki & Stixrude 1999) on magnesiowüstite (for Fe) and perovskite (for Ti) show that the presence of iron-enriched minerals increases the density of the rock, but lowers its V_p and V_s, which in

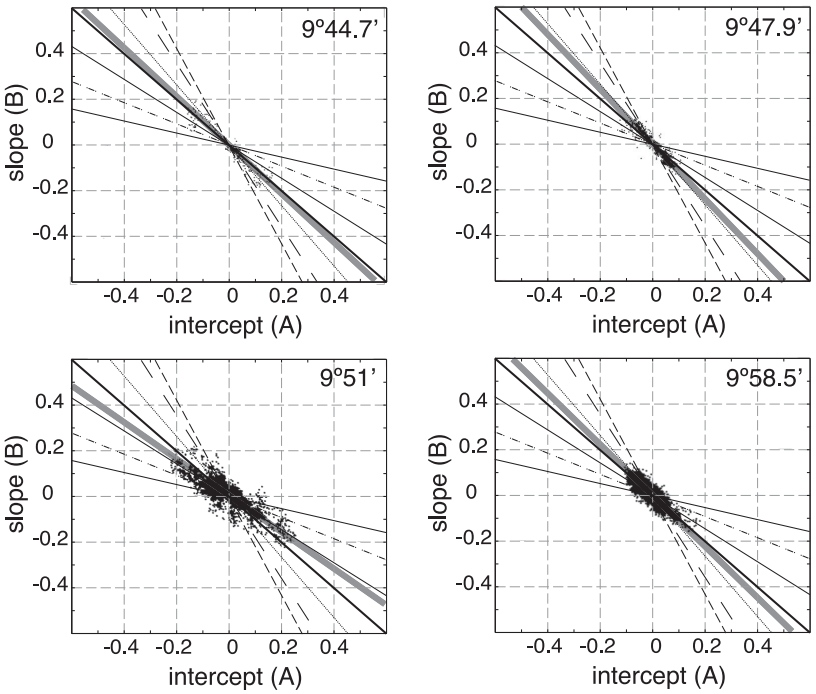

Figure 9. AVA crossplots obtained for four AML discontinuities encountered within and at the edges of the seafloor extent of the 2005–2006 eruption lava flow, centred at 9°44.7′N (between segments 5 and 6; CRP range 16 773–16 870), at 9°47.9′N (between segments 6 and 7; CRP range 17 748–17 796), at 9°51′N (between segments 7 and 8; CRP range 18 597–18 790), at 9°56.2′N (between segments 8 and 9; CRP range 20 156–20 350). The best-fit trend is plotted with a thick solid grey line. Calculated trend lines from the template in Fig. 4 are shown in black.

theory, could potentially lead to higher values of attributes *A* and *B* (in absolute value).

Segments located north and south of the 2005–2006 lava flow (segments 1, 2, 3, 4, 5 and 9). Of the remaining segments, segment 3 is the only one that on the segment-length scale shows a similar AVA response (mostly molten) to the segments located within the eruption area (segments 6, 7 and 8; Fig. 10a). At a fine scale, segment 3 is mostly to highly molten along most of its length (Fig. 10c), and only its northernmost part is partially molten. It is interesting to note that within this segment variations in melt content occur in short bands (<500 m long), which are somewhat shorter than those observed within the eruption area. In contrast to the mostly molten segments, segments that have end-member behaviour (partially or highly molten) on the segment scale exhibit less variation in melt content on a fine scale (Fig. 10c). For instance, segment 5 (identified as highly molten from the segment-scale analysis) displays an ∼1700 m long, highly molten region at its centre, whereas near both northern and southern extremities, predominantly partially molten regions are inferred. Similar results are obtained for the segments that are, on average, partially molten, that is segment 9 (Fig. 10b) and segment 2 (Fig. 10c): these two segments are inferred to be partially molten, except for narrow patches within segments centres where mostly to highly molten regions are inferred (∼600 m long). Segment 1 displays hardly any variation in melt content; it is mostly partially molten along its entire length.

AML discontinuity regions. AML discontinuity regions present within our survey area range in length from ∼0.125 to 1.2 km. For most of them, AVA crossplotting indicates they are partially molten regions (Figs 9 and 10b,c). There are two exceptions. First, the discontinuity region centred at 9°51′N displays an average $\langle V_p \rangle / \langle V_s \rangle$ of 2.11 (Fig. 9; Table 3), suggesting the presence of mostly to highly molten material. Higher melt content there may be related to the presence of a wide, westward dipping portion of the AML as imaged in the 3-D cross-axis data set (Carton *et al.* 2014), as this deeper extension of the magma body to the west may provide a pathway for additional melt influx to the AML in the region around the AML discontinuity. Moreover, at 9°51.2′N the on-bottom geodesy study of Nooner *et al.* (2014) provided evidence for inflation of the seafloor of up to 12 cm from 2009 December to 2011 October, corresponding to a source at 2.7 km depth beneath the ridge axis, within this discontinuity region. The other exception is the AML discontinuity centred at 9°37.8′N for which AVA crossplotting results show the presence of molten material in its northernmost part. However, its southernmost part (∼300 m in length) exhibits significant scattering in the crossplots, preventing derivation of a meaningful trend line (Fig. 10c).

5 DISCUSSION

5.1 Comparison with earlier seismic constraints on AML melt distribution

5.1.1 Comparison with partial-offset stacking results

On the individual segment-length scale there is generally a good agreement between the results obtained from partial-offset stacking and results from the *A* versus *B* crossplotting method (Figs 5b–d and 10a). For instance, the crossplot for segment 5 displays the largest $\langle V_p \rangle / \langle V_s \rangle$, indicative of high melt content, consistent with the presence of a prominent $P_{AML}S$ phase in this region. For segment 4, where the low $\langle V_p \rangle / \langle V_s \rangle$ indicates a lens with a higher crystallinity, partial-offset stacking results show a weak $P_{AML}S$.

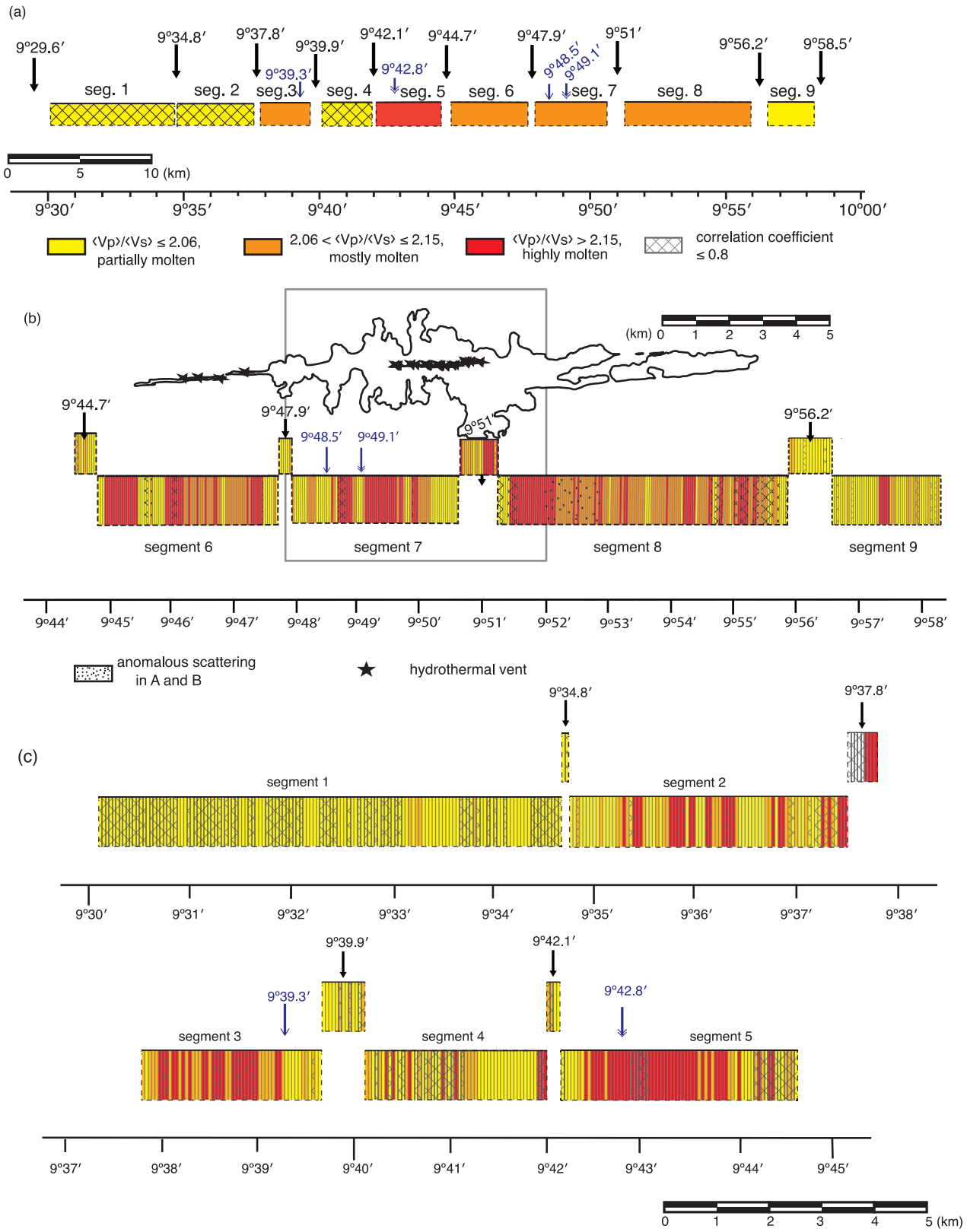

Figure 10. (a) Schematic summary of along-axis variations in melt content of the AML from AVA crossplotting analysis. Results are shown for the nine individual segments between 9°29.8′ and 9°58.4′N. Black arrows indicate fine-scale segmentation in AML (Carbotte *et al.* 2013). As in Fig. 1, double-headed blue arrows show locations of 1-D waveform inversion study of Xu *et al.* (2014) and the single-headed ones locations of 1-D waveform inversion studies of Collier & Singh (1997, 1998). Correlation coefficient is given in absolute value. (b) Results from finer-scale analysis (conducted on groups of 10 adjacent CRPs, that is ∼62.5 m long sections) for AML segments (segments 6, 7 and 8) located vertically beneath the 2005–2006 eruption lava flow and segment 9 just north of the eruption area. The grey rectangle marks the region within which the volume calculations represented in Table B1 are done. Legend is shown below with the remaining items as in (a). (c) Fine-scale analysis results for AML segments 1, 2, 3, 4 and 5 and intervening AML discontinuity regions. All the elements and symbols are the same as in (a).

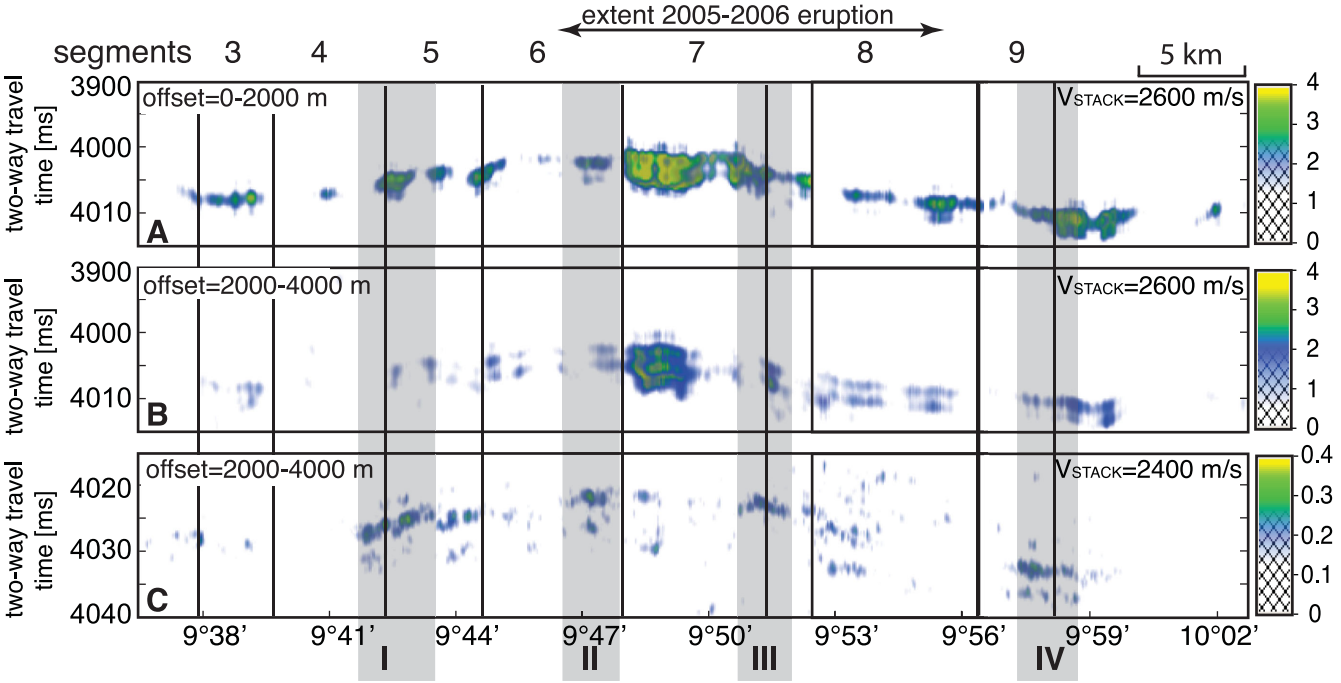

Figure 11. Partial offset stacks from Fig. 6 in Xu *et al.* (2014). Energy attribute of whole post-stack time-migrated along-axis swath volumes is shown, projected onto ridge-axis centred in-lines. Panels A, B, C show near-offset $P_{AML}P$, far-offset $P_{AML}P$, and far-offset $P_{AML}S$ stacks, respectively. Grey shading indicates regions interpreted as melt-rich sections by Xu *et al.* (2014). The original figure is modified to fit the orientation, scale and labels in our Fig. 5.

However, there are locations where the two methods provide contradictory indications. Along segment 9, the *A* versus *B* crossplotting gives $\langle V_p \rangle / \langle V_s \rangle \leq 2.06$ (Fig. 8) thus indicating a partially molten AML, but a relatively strong $P_{AML}S$ phase is observed at mid-offsets (Fig. 5d), which would suggest a melt-rich segment. Such contradictory results may be rooted in the fact that the signal-to-noise ratio for the $P_{AML}P$ phase is small at all offsets in this region, hence a somewhat ambiguous AVA behaviour.

While the $P_{AML}S$ partial offset stacks provide a qualitative view of regional variations in melt content within the AML, the advantage of the AVA technique is that it can resolve fine-scale variations in AML melt content within each individual AML segment (Fig. 10b). Moreover, the crossplotting method allows organization and display of information derived from the partial-angle stacks for a whole segment quantified by the trend line (Fig. 8), whereas the partial-offset stacking method relies only on qualitative estimate of relative change in amplitude strength between the segments (Fig. 5).

Xu *et al.* (2014) also performed partial-offset stacking between 9°30′N and 10°N using the entire along-axis data swath acquired (maximum width ∼900 m) binned in 3-D and calculated stacked $P_{AML}S$ energy across the width of the swath (Fig. 11). The authors interpreted as melt-rich the regions of strongest stacked (across the width of the swath) $P_{AML}S$ energy. These are: I—the northernmost portion of segment 4 spanning the 9°42.1′N discontinuity and the southern half of segment 5; II—the northern half of segment 6; III—the northern half of the 9°51′N discontinuity along with the first ∼1.4 km of segment 8; IV—most of segment 9 (excluding the first 1.2 km) and discontinuity 9°58.5′N. Overall, the results from our partial offset stacks for the innermost axial zone agree with the results of Xu *et al.* (2014; compare Figs 5b–d and 11). However, as the analysis of Xu *et al.* (2014) stacks data across the width of the AML incorporating the cross-axis variability of the AML, mixing signals from oblique-trending discontinuity and mid-segments zones, detailed comparison is not possible.

5.1.2 *Comparison with 1-D waveform inversion results*

Results obtained from the fine-scale crossplotting analysis (Fig. 10b) are in agreement with results from 1-D waveform inversion performed at two contrasting locations using CMP supergather data from the same 2008 survey (Xu *et al.* 2014). Waveform inversion results indicate that the AML at 9°42.8′N is best modelled with a low V_p (2.95–3.23 km s^{-1}) and low V_s (0.3–1.5 km s^{-1}), indicating >70 per cent melt fraction. This CMP supergather is located within segment 5, for which we obtain $\langle V_p \rangle / \langle V_s \rangle = 2.19$, that is in the highly molten range. At 9°49.1′N, Xu *et al.* (2014) estimate higher V_p (4.52–4.82 km s^{-1}) and V_s (2.0–3.0 km s^{-1}) within the AML, which they attribute to <40 per cent melt fraction. This second CMP supergather is situated within a short (∼190 m) section with $\langle V_p \rangle / \langle V_s \rangle = 1.97$, which we interpret as a partially molten region of the AML (Fig. 10b). It is noteworthy that our fine-scale analysis shows that this short section is bounded on either side with longer (>500 m) AML sections showing higher melt content (Fig. 10b). Hence in this region, the 1-D waveform inversion results appear to be representative of only a very small section of the AML. This comparison highlights the need to exercise caution in the extrapolation of point-location results from 1-D studies.

Other 1-D waveform modelling and inversion results in the area were obtained using data from the 1985 survey (Hussenoeder *et al.* 1996; Collier & Singh 1997, 1998), and thus provide characterization of the AML prior to both the 1991–1992 and 2005–2006 eruptions. At 9°48.5′N the AML was found to be best modelled with $V_s \leq 1$ km s^{-1}, indicating high melt fraction (Collier & Singh 1998). Crossplotting of the 2008 data (acquired ∼2 yr after the last

documented eruption) indicates however a partially molten AML at this latitude (Fig. 10b). This location is within the southern part of the wide 2005–2006 lava flow region. Hence, one could speculate that temporal variations in melt content at the AML inferred from comparison of these two studies might be related to melt drainage during the two eruption episodes.

At 9°39.3′N using 1-D full waveform inversion Collier & Singh (1997) obtained *S*-wave velocity $V_s \leq 1$ km s^{-1} as the best fit, indicative of molten AML. In contrast, using forward waveform modelling, combined with amplitude variation with slowness (based on curve-fitting) Hussenoeder *et al.* (1996) at the same location obtained $V_s > 1.2$ km s^{-1} and concluded the presence of a more crystalline AML. The most plausible explanation for the differences in melt content obtained by these two earlier studies (Collier & Singh 1997; Hussenoeder *et al.* 1996) that used subsets of the same 1985 profile resides in differences in chosen methodologies and associated limitations. Our fine-scale analysis shows that the 9°39.3′N point location falls at the boundary between regions of the AML with contrasting properties (Fig. 10c), partially molten to the north and mostly molten to the south.

5.1.3 *Additional remarks*

The intercept versus slope crossplotting method is based on the two-term Shuey's approximation of the *P*-wave reflection coefficient equation, which is valid for incidence angles up to 30° (Shuey 1985; see Appendix A). For an AML at ∼1.5 km (average depth of the AML within the area of interest) below the seafloor this corresponds to a maximum offset of ∼2.8 km (Fig. 6). Hence, the data recorded on the outer half of our 6-km-long streamers, including the offset range where *P*-to-*S* converted phases from the AML are observed, is not used for the AVA analysis carried out in this study. This point merits discussion since waveform inversion studies of AML structure have generally argued that inversion results are better constrained when *S*-wave information is included, which requires data recorded at offsets of >∼3 km (e.g. Collier & Singh 1997; Singh *et al.* 1999). Our results suggest that the $P_{AML}P$ phase, at incidence angles up to 30°, also contains the information necessary to extract $\langle V_p \rangle / \langle V_s \rangle$ reliably through stacking over two distinct angle domains. One important difference between the AVA crossplotting approach used here and waveform inversion is that waveform inversion provides the detailed velocity structure for the AML (and information on its roof and floor structure), whereas only the $\langle V_p \rangle / \langle V_s \rangle$ ratio across the interface is characterized when performing AVA crossplotting. On the other hand, AVA crossplotting allows for a more efficient analysis of 2-D or 3-D seismic data sets than waveform-fitting methods. In addition, the AVA crossplotting approach is more quantitative than partial-offset *P*-wave stacking followed by visual inspection or graphic rendering of the results (e.g. Singh *et al.* 2006).

Thinning of the AML is expected to be associated with smaller amount of melt and higher connectivity between crystals. Simple 1-D synthetic tests (Marjanović 2013) show that thinning of the AML would affect the AVA response in such a way that in absolute value intercept (A) would decrease and slope (B) would increase, resulting in a lower $\langle V_p \rangle / \langle V_s \rangle$. In our interpretation scheme, a lower $\langle V_p \rangle / \langle V_s \rangle$ is interpreted as arising from an AML with higher crystalline fraction. Therefore, although our methodology is not able to unravel the contribution of variations in AML thickness to the AVA response, the result (higher crystallinity inferred in case of a thinner AML) remains consistent with the physical conditions that accompany the presence of a thin lens.

5.2 Relationships with magmatic, volcanic and hydrothermal processes

Our fine-scale AVA analysis of the AML beneath the EPR suggest short length scales of melt-mush variations within AML segments, possibly <100 m but more generally on the order of a few 100s of metres. There is thus strong indication that these AML segments, which have been identified from AML geometry and disruptions in continuity, are not homogeneous bodies. Furthermore, AML portions with high crystallinity, such as those imaged beneath the central region of the 2005–2006 eruption, are unlikely to convect vigorously, contrary to AML portions with high melt content (e.g. Brandeis & Jaupart 1986).

5.2.1 *Signature of the 2005–2006 eruption*

In the following discussion we assume that the state of the AML imaged in 2008 is representative of that present at the end of the eruption in 2006. Although we cannot rule out some magma mixing, replenishment, and withdrawal in the 2 yr between the eruption and the time of our survey, we make the simplifying assumption that the melt distribution within the AML in 2008 primarily reflects the magma withdrawal effects of the 2005–2006 eruption. From our detailed AVA results, the three AML segments underlying the area of erupted lava show variable melt content, with 25 per cent of their total length being interpreted as solid to mushy, 37 per cent percent mostly molten and 38 per cent highly molten (excluding discontinuity zones). Most of the partially molten portion is present within the central segment (segment 7) which is believed to encompass the primary eruption site for the event (Fundis *et al.* 2010): within this segment, ∼45 per cent of its total length is partially molten, compared to 15 and 24 per cent of segments 6 and 8, respectively. The above observation is consistent with the preferred eruption scenario of Xu *et al.* (2014) in which the authors assume that the eruption drained most of the melt in this central segment (segment 7), while the AML segments located immediately to the north (segment 8) and to the south (segment 6) remained mostly molten.

Owing to the lack of detailed constraints on the total volume of the AML located below the eruption area (the areal extent of the AML is well mapped by Carton *et al.* 2014, but spatial variations in thickness of the lens are unknown) and the lack of information on the pre-eruption volume of melt within them, any estimate of the fraction of available melt stored in the AML that erupted is highly speculative. However, our ballpark estimate of the possible melt volume stored in the AML in the 9°47.9–52′N area (13.3×10^6 m^3; see Appendix B for detailed explanation behind the calculation) is smaller than the estimate (based on seafloor mapping) of the volume of extruded lava emplaced within the same region (18.2×10^6 m^3). To account for this discrepancy, the missing magma volume could have been supplied from deeper melt sources. Indeed, a growing body of evidence suggests that the 2005–2006 eruption involved melt extraction from deeper crustal and/or uppermost mantle sources and that this deeper supply was focused beneath the central magma lens (Goss *et al.* 2010; Wanless & Shaw 2012; Moore *et al.* 2014; Zha *et al.* 2014). Marjanović *et al.* (2014) demonstrated the presence of sub-AML events that they interpret as mid-crustal magma lenses, providing support for a model of multiple-sill crustal accretion. The longest partially molten AML section identified within the central eruption

site (∼800 m in length, extending between 9°50.2′ and 9°50.65′N), is located above a prominent gap in the sub-AML reflections, which is attributed by Marjanović *et al.* (2014) to localized drainage of melt from both the sub-AML and AML events. We cannot exclude the possibility that prior to the eruption magma was mobilized from even deeper sources (as suggested by Moore *et al.* 2014), such as the ones revealed at 4–7 km depth at 9°48′N and 9°33′N by compliance data (Zha *et al.* 2014). Based on petrologic studies of the erupted lavas, Moore *et al.* (2014) conclude that the predominant mechanism for triggering the 2005–2006 eruption event may have been a focused pulse of primitive magma mobilized from deeper sources, migrating to the AML beneath the central eruption site just prior to the eruption. The above explanations are not mutually exclusive, and melt from multiple levels within the magmatic system may have contributed to the eruption.

5.2.2 Relationship between melt content and presence and distribution of high-temperature vents

The presence of an AML beneath the ridge crest is considered a necessary but not sufficient element for sustaining high-temperature hydrothermal systems (e.g. Baker 2009). For such systems to develop and persist for decades, several additional conditions need to be met. First, the upper crust needs to maintain permeable pathways. Second, the 50–60-m-thick high-velocity AML lid (Singh *et al.* 1999) that forms the conductive boundary layer for hydrothermal circulation needs to remain thin, and this may be achieved through seismogenic cracking associated with magma recharge processes (Wilcock *et al.* 2009). Replenishment of the AML is also essential to maintaining the heat source, with the available melt in the AML otherwise freezing on timescales of years to decades (e.g. Liu & Lowell 2009) or centuries in a moderate permeability setting (Fontaine *et al.* 2011).

From studies of melt-mush segmentation on the ultrafast-spreading southern EPR in the 14°S area and the Cleft segment on the intermediate spreading Juan de Fuca Ridge, Singh *et al.* (1999) and Canales *et al.* (2006), respectively, proposed that high-temperature hydrothermal vents are preferentially located above melt-rich sections of the AML and that only melt-rich lenses are able to support vigorous, long-lasting venting. The suggestion by Wilcock *et al.* (2009) that the stresses induced by magma recharge push the AML lid upwards and create new cracks that prevent thickening of the conductive boundary layer is consistent with this hypothesis. However, a compilation of existing hydrothermal plume locations and AML data by Baker (2009) concludes that while high-temperature vents are almost always found where there is a seismically imaged AML, the correlation with melt fraction is less clear: vigorous plumes have also been detected above AML sections not characterized as melt-rich (Cleft segment), and some melt-rich lenses support 'unremarkable' plume activity (Southern EPR 14°S).

Likewise, our results from the 9°30′-10°N area suggest that there is no consistent relationship between the melt content of the AML imaged in 2008 and presence of high-temperature vents at the seafloor. The majority of modern vents north of 9°10′N, as identified in the ∼20 yr prior to our survey (Haymon *et al.* 1991; Von Damm 2004) as well as those presumed to be active in 2008 (documented by the numerous vent sampling cruises in the years following the eruption and spanning our survey, Fornari *et al.* 2012), are concentrated above moderate melt content segments 6 and 7. In comparison, none are observed above segment 8, although this segment shows a similar melt content to segments 6 and 7 (Fig. 10b). No hydrothermal vents have been observed within segment 5, whereas this segment has the highest inferred melt content of all nine AML segments analysed. Two black smokers (M and Q) near latitude 9°50.75′N became inactive following the 2005–2006 eruption (Von Damm 2006; Fornari *et al.* 2012), but they overlie a zone of high melt fraction imaged from our 2008 data. Assuming our data is representative of the state of the AML post-eruption, when these vents became extinct, factors other than changes in heat output of the melt body below are likely to have given rise to the demise of these vents, such as changes in fluid flow pathways within the crustal lid above the magma reservoir.

As noted by Baker (2009), differing timescales of melt withdrawal from and recharge to the AML and hydrothermal processes may be at play. Fluid pathways in the upper crust are expected to evolve, opening in response to cracking and ongoing fluid flow, clogging and closing with cooling and hydrothermal precipitation. The hydrothermal system can react very quickly to changes in heat source distribution, such as a dyke intrusion event (e.g. Von Damm 1995; Fornari *et al.* 1998b; Sohn *et al.* 1998), which also induces a rapid change in upper crustal permeability. However, the extinction of high-temperature vents and the establishment of new vent sites in response to changes in melt content and/or available melt volume at the AML at depth may operate over longer timescales. Investigation of the temporal interactions between the magmatic and hydrothermal system would require the seismic determination of melt-mush segmentation at close repeat intervals, with simultaneous monitoring of the hydrothermal system (e.g. of microseismicity, fluid flux and vent temperatures), which has not been done on any spreading centre system so far.

6 CONCLUSIONS

Here, for the first time, we apply an industry-type *A* versus *B* cross-plotting technique to a crystalline crust environment to examine variations in melt fraction along the axis of the northern EPR from 9°29.6 to 9°58.5′N, encompassing nine fine-scale AML segments. Results for segments centred at 9°32.4′, 9°36.2′, 9°41′N and 9°57.4′ (segments 1, 2, 4 and 9, respectively) indicate a partially molten AML. The AML segment centred at 9°38.7′, as well as the three segments that underlie the recent eruption area (segments 6–8, centred at 9°46.3′, 9°49.3′ and 9°53.6′N, respectively) are characterized as mostly molten on average, with the segment centred at 9°43.3′ (segment 5, south of the eruption area), displaying the highest average melt content.

Our detailed AVA analyses conducted at 62.5 m interval show that the AML melt content varies at spatial scales much smaller than the length of the fine-scale AML segments identified from the geometry of this body. The above suggests a rather heterogeneous distribution of melt and limited magma mixing within a single AML segment, from this snapshot obtained ∼2 yr after the 2005–2006 eruption event. By making simple assumptions on the AML geometry and feeder dyke dimensions and by considering melt extraction from only partially to mostly molten portions of the AML segments underlying the lava flow on the seafloor, we suggest that the volume of available melt within the AML underlying the 9°47.9–52′N area would not have been sufficient to erupt the corresponding portion of the flow. Within this region, the primary eruptive site at ∼9°50.4′N is located above an ∼800 m long partially molten section of the AML, itself underlain by a prominent gap in the sub-AML magma lenses (Marjanović *et al.* 2014), and we suggest that additional melt for the eruption was sourced from such deeper magma sills. On the

basis of this 2 yr post-eruption snapshot, no evident spatial correlation is observed between portions of the AML characterized by a low crystalline component and the presence of high-temperature hydrothermal vents. Differing timescales for magmatic and hydrothermal processes may be at play, in relation with the evolution of fluid flow pathways within the crustal lid above the magma reservoir.

In general, the results obtained by application of the AVA crossplotting method agree with the results obtained from stacking of the *P*-to-*S* converted phase and 1-D waveform inversion applied on the same data set (Xu *et al.* 2014). Our study shows that the AVA crossplotting method represents an efficient approach for providing relative variations in melt distribution for large regions and complements results obtained from the $P_{\mathrm{AML}}S$ approach, providing information on melt content variations at very small spatial scale that may not be apparent on partial stack sections.

Our current application of the method using a 2-D data set is limited in the physical characteristics of the AML that can be extracted given the highly 3-D nature of this body. However, analysis and results presented here suggest the *A* versus *B* crossplotting technique is a promising tool for the study of MOR magma systems.

ACKNOWLEDGEMENTS

We thank members of the ConocoPhillips Subsurface Technology Team for help in establishing the data preparation flow. Jeff Malloy, Mark Wuenscher and Bob Olsen are gratefully acknowledged for their effort and time. We thank Douglas Foster (ConocoPhillips), Leon Barens (Total) and Stefan Hussenoeder (ExxonMobil) for their insight on the AVA method and its interpretation. Douglas Foster and Bill Lucas are gratefully acknowledged for providing the ABAVO crossplotting tool within the GeoCraft© software developed by ConocoPhillips. Seismic data processing was done using Landmark and Paradigm softwares. We thank Jenny Collier and Daniel J. Fornari for insightful discussions and comments. This research was supported by NSF awards OCE0327872 to J.C.M. and S.M.C., OCE-0327885 to J.P.C., and OCE0624401 to M.R.N.

REFERENCES

Aghaei, O., Nedimović, M.R., Carton, H., Canales, J.P., Carbotte, S.M. & Mutter, J.C., 2014. Crustal thickness and Moho character from poststack-migrated 3D MCS data collected over the fast-spreading East Pacific Rise from 9°42′N to 9°57′N, *Geochem. Geophys. Geosyst.,* **15,** 634–657.

Aki, K.I. & Richards, P.G., 1980. *Quantitative Seismology,* W. H. Freeman and Co.

Arnulf, A.F., Harding, A.J., Kent, G.M., Carbotte, S.M., Canales, J.P. & Nedimović, M.R., 2014. Anatomy of an active submarine volcano, *Geology,* **42**(8), 655–658.

Baker, E.T., 2009. Relationships between hydrothermal activity and axial magma chamber distribution, depth, and melt content, *Geochem. Geophys. Geosyst.,* **10,** Q06009, doi:10.1029/2009GC002424.

Bakke, N.E. & Ursin, B., 1998. Thin-bed AVO effects, *Geophys. Prospect.,* **46**(6), 571–587.

Bortfeld, R., 1961. Approximation to the reflection and transmission coefficients of plane longitudinal and transverse waves, *Geophys. Prospect.,* **9,** 485–503.

Brandeis, G. & Jaupart, C., 1986. On the interaction between convection and crystallization in cooling magma chambers, *Earth planet. Sci. Lett.,* **77,** 345–361.

Canales, J.P. *et al.*, 2006. Seismic evidence for variations in axial magma chamber properties along the southern Juan de Fuca Ridge, *Earth planet. Sci. Lett.,* **246,** 353–366.

Canales, J.P. *et al.*, 2012a. Network of off-axis melt bodies at the East Pacific Rise, *Nat. Geosci.,* **5**(4), 279–283.

Canales, J.P., Carton, H., Mutter, J.C., Harding, A., Carbotte, S.M. & Nedimović, M.R., 2012b. Recent advances in multichannel seismic imaging for academic research in deep oceanic environments, *Oceanography,* **25**(1), 113–115.

Carazzone, J.J. & Srnka, L.J., 1993. Elastic inversion of Gulf of Mexico data, in *Offset Dependent Reflectivity—Theory and Practice of AVO Analysis,* pp. 303–313, eds Castagna, J.P. & Backus, M.M., Society of Exploration Geophysicists.

Carbotte, S. & Macdonald, K., 1992. East Pacific Rise 8°–10°30′N: evolution of ridge segments and discontinuities from SeaMARC II and three-dimensional magnetic studies, *J. geophys. Res.,* **97**(B5), 6959–6982.

Carbotte, S.M., Marjanović, M., Carton, H., Mutter, J.C., Canales, J.P., Nedimović, M.R., Han, S. & Perfit, M.R., 2013. Fine-scale segmentation of the crustal magma reservoir beneath the East Pacific Rise, *Nat. Geosci.,* **6,** 866–870.

Caress, D.W., Burnett, M.S. & Orcutt, J.A., 1992. Tomographic image of the axial-low velocity zone at 12°50′N on the East Pacific Rise, *J. geophys. Res.,* **97,** 9243–9264.

Carton, H.D., Carbotte, S.M., Mutter, J.C., Canales, J.P. & Nedimović, M.R., 2014. Axial magma system geometry beneath a fast-spreading mid-ocean ridge: insight from three-dimensional seismic reflection imaging on the East Pacific Rise 9°42 to 9°57′N, Abstract V22A-02 presented at 2014 Fall Meeting, AGU, San Francisco, Calif., 15–19 Dec.

Castagna, J.P., 1993. AVO analysis—tutorial and review, in *Offset Dependent Reflectivity—Theory and Practice of AVO Analysis,* pp. 3–36, eds Castagna, J.P. & Backus, M.M., Society of Exploration Geophysicists.

Castagna, J.P. & Swan, H.W., 1997. Principles of AVO crossplotting, *TLE, Soc. Explor. Geophys.,* **17,** 337–342.

Castagna, J.P., Swan, H.W. & Foster, D.J., 1998. Framework for AVO gradient and intercept interpretation, *Geophysics,* **63**(3), 948–956.

Collier, J.S. & Singh, S.C., 1997. Detailed structure of the top of the melt body beneath the East Pacific Rise at 9°40′N from waveform inversion of seismic reflection data, *J. geophys. Res.,* **102**(B9), 20 287–20 304.

Collier, J.S. & Singh, S.C., 1998. A seismic inversion study of the axial magma chamber reflector beneath the East Pacific Rise near 10°N, in *Modern Ocean Floor Processes and the Geological Record,* pp. 17–28, eds Mills, R.A. & Harrison, K., Geological Society.

Cowen, J.P. *et al.*, 2007. Volcanic eruptions at East Pacific Rise near 9°50′N, *EOS, Trans. Am. geophys. Un.,* **88**, 81–83.

Demirbag, E., Coruh, C. & Costain, J.K., 1993. Inversion of *P*-wave AVO, in *Offset-Dependent Reflectivity—Theory and Practice of AVO Analysis,* pp. 500–540, eds Castagna, J.P. & Backus, M.M., Society of Exploration Geophysicists.

Detrick, R.S., Buhl, P., Vera, E.E., Mutter, J.C., Orcutt, J.A., Madsen, J.A. & Brocher, T.M., 1987. Multi-channel seismic imaging of a crustal magma chamber along the East Pacific Rise, *Nature,* **326,** 35–41.

Detrick, R.S., Harding, A.J., Kent, G.M., Orcutt, J.A., Mutter, J.C. & Buhl, P., 1993. Seismic structure of the Southern East Pacific Rise, *Science,* **259,** 499–503.

Fontaine, F.J., Olive, J.-A., Cannat, M., Escartin, J. & Perol, T., 2011. Hydrothermally-induced melt lens cooling and segmentation along the axis of fast- and intermediate-spreading centers, *Geophys. Res. Lett.,* **38,** L14307.

Fornari, D.J. *et al.*, 1998a. Time-series temperature measurements at high-temperature hydrothermal vents, East Pacific Rise 9°49′–51′N: evidence for monitoring a crustal cracking event, *Earth planet. Sci. Lett.,* **160,** 419–431.

Fornari, D.J., Haymon, R.M., Perfit, M.R., Gregg, T.K.P. & Edwards, M.H., 1998b. Axial summit trough of the East Pacific Rice 9°–10°N: geological characteristics and evolution of the axial zone on fast spreading mid-ocean ridge, *J. geophys. Res.,* **103,** 9827–9855.

Fornari, D.J., 2004. Submarine lava flow emplacement at the East Pacific Rise 9°50′N: implications for the uppermost ocean crust stratigraphy and hydrothermal fluid circulation, in *The Thermal Structure of the Ocean Crust and the Dynamics of Hydrothermal Circulation,* pp. 187–217, eds German, C.R. *et al.*, AGU.

Fornari, D.J., Beaulieu, S.E., Holden, J.F., Mullineaux, L.S. & Tolstoy, M., 2012. Introduction to the special issue: from RIDGE to Ridge 2000, *Oceanography,* **25**(1), 12–17.

Foster, D.J. & Mosher, C.C., 1992. Suppression of multiple reflections using the Radon transform, *Geophysics,* **57,** 386–395.

Foster, D.G., Keys, R.G. & Schmitt, D.P., 1997. Detecting subsurface hydrocarbons with elastic wavefields, in *Inverse Problems in Wave Propagation,* pp. 195–218, eds Chavent, G., Papanicolaou, G., Sacks, P. & Symes, W., Springer-Verlag.

Foster, D.J., Keys, R.G. & Lane, F.D., 2010. Interpretation of AVO anomalies, *Geophysics,* **75**(5), 75A3–75A13.

Fundis, A.T., Soule, S.A., Fornari, D.J. & Perfit, M.R., 2010. Paving the seafloor: volcanic emplacement processes during the 2005–2006 eruptions at the fast spreading East Pacific Rise, 9°50′N, *Geochem. Geophys. Geosyst.,* **11,** Q08024, doi:10.1029/2010GC003058.

Goss, A.R., Perfit, M.R., Ridley, W.I., Rubin, K.H., Kamenov, G.D., Soule, S.A., Fundis, A. & Fornari, D.J., 2010. Geochemistry of lavas from the 2005–2006 eruption at the East Pacific Rise, 9°46′N–9°56′N: implications for ridge crest plumbing and decadal changes in magma chamber compositions, *Geochem. Geophys. Geosyst.,* **11,** Q05T09, doi:10.1029/2009GC002977.

Gregg, T.K.P., Fornari, D.J., Perfit, M.R., Haymon, R.M. & Fink, J.H., 1996. Rapid emplacement of a mid-ocean ridge lava flow on the east Pacific Rise at 9°46–51′N, *Earth planet. Sci. Lett.,* **144,** E1–E7.

Han, S., Carbotte, S.M., Carton, H., Mutter, J.C., Aghaei, O., Nedimović, M.R. & Canales, J.P., 2014. Architecture of off-axis magma bodies at EPR 9°37–40′N and implications for oceanic crustal accretion, *Earth planet. Sci. Lett.,* **390,** 31–44.

Harding, A.J., Orcutt, J.A., Kappus, M.E., Vera, E.E., Mutter, J.C., Buhl, P., Detrick, R.S. & Brocher, T.M., 1989. The structure of young oceanic crust at 13°N on the East Pacific Rise from expanding spread profiles, *J. geophys. Res.,* **94,** 12 163–12 196.

Hashin, Z. & Shtrikman, S., 1963. A variational approach to the theory of the elastic behaviour of multiphase materials, *J. Mechan. Phys. Solids,* **11**(2), 127–140.

Haymon, R.M. *et al.*, 1993. Volcanic eruption of the mid-ocean ridge along the East Pacific Rise crest at 9°45–52′N: direct submersible observations of seafloor phenomena associated with an eruption event in April, 1991, *Earth planet. Sci. Lett.,* **119,** 85–101.

Haymon, R.M., Fornari, D.J., Edwards, M.H., Carbotte, S., Wright, D. & Macdonald, K.C., 1991. Hydrothermal vent distribution along the East Pacific Rise Crest (9°09′–54′N) and its relationship to magmatic and tectonic processes on fast-spreading mid-ocean ridges, *Earth planet. Sci. Lett.,* **104,** 513–534.

Herron, T.J., Ludwig, W.J., Stoffa, P.L., Kan, T.K. & Buhl, P., 1978. Structure of the East Pacific Rise Crest from multichannel seismic reflection data, *J. geophys. Res.,* **83**(B2), 798–804.

Herron, T.J., Stoffa, P.L. & Buhl, P., 1980. Magma chamber and mantle reflections – East Pacific Rise, *Geophys. Res. Lett.,* **7**(11), 989–992.

Hilterman, F.J., 2001. *Seismic Amplitude Interpretation, Distinguished Instructor Short Course,* Distinguished Instructor Series, No. 4, Society of Exploration Geophysicists and European Association of Geoscientists and Engineers.

Hussenoeder, S.A., Collin, J.A., Kent, G.M., Detrick, R.S. & the TERA Group, 1996. Seismic analysis of the axial magma chamber reflector along the southern East Pacific Rise from conventional reflection profiling, *J. geophys. Res.,* **101**(B10), 22 087–22 105.

Juhlin, C. & Young, R. 1993. Implications of thin layers for amplitude variation with offset (AVO) studies, *Geophysics,* **58**(8), 1200–1204.

Kallweit, R.S. & Wood, L.C., 1982. The limits of zero-phase wavelets, *Geophysics,* **47,** 1035–1046.

Karki, B.B. & Stixrude, L., 1999. Seismic velocities of major silicate and oxide phases of the lower mantle, *J. geophys. Res.,* **104**(B6), 13 025–13 033.

Kent, G.M., Harding, A.J. & Orcutt, J.A., 1990. Evidence for a smaller magma chamber beneath the East Pacific Rise at 9°30′N, *Nature,* **344,** 650–653.

Kent, G.M., Harding, A.J. & Orcutt, J.A., 1993a. Distribution of magma beneath the East Pacific Rise between the Clipperton transform and the 9°17′N deval from forward modeling of common depth point data, *J. geophys. Res.,* **98**(B8), 13 945–13 969.

Kent, G.M., Harding, A.J. & Orcutt, J.A., 1993b. Distribution of magma beneath the East Pacific Rise near the 9°03′N overlapping spreading center from forward modeling of common depth point data, *J. geophys. Res.,* **98,** 13 971–13 995.

Knapp, R.W., 1991. Fresnel zones in light of broadband data, *Geophysics,* **56,** 354–359.

Lin, T.L. & Phair, R., 1993. AVO tuning, *63rd Annual International Meeting,* Society of Exploration Geophysics, Expanded Abstract, pp. 727–730.

Lindsey, J.P., 1989. The Fresnel zone and its interpretive significance, *The Leading Edge,* **10,** 33–39.

Liu, Y. & Schmitt, D.R., 2003. Amplitude and AVO responses of a single thin bed, *Geophysics,* **68**(4), 1161–1168.

Liu, L. & Lowell, R.P., 2009. Models of hydrothermal heat output from a convecting, crystallizing, replenished magma chamber beneath an oceanic spreading center, *J. geophys. Res.,* **114,** B02102, doi:10.1029/2008JB005846.

Macdonald, K.C. *et al.*, 1992. The East Pacific Rise and its flanks 8–18°N: history of segmentation, propagation and spreading direction based on SeaMARC II and Sea Beam studies, *Marine Geophys. Res.,* **14,** 299–344.

Marjanović, M., 2013. Signature of present and past melt distribution at fast and intermediate spreading centers, *PhD thesis,* Columbia University, New York.

Marjanović, M., Carbotte, S.M., Carton, H., Nedimović, M.R., Mutter, J.C. & Canales, J.P., 2014. A multi-sill magma plumbing system beneath the axis of the East Pacific Rise, *Nature Geosci.,* **7,** doi:10.1038/ngeo2272.

Moore, A., Coogan, L.A., Costa, F. & Perfit, M.R., 2014. Primitive melt replenishment and crystal-mush disaggregation in the weeks preceding the 2005–2006 eruption 9°50′N EPR, *Earth planet. Sci. Lett.,* **403,** 15–26.

Murase, T. & McBirney, A.R., 1973. Properties of some common igneous rocks and their melts at high temperatures, *Geol. Soc. Am. Bull.,* **84,** 3563–3592.

Mutter, J.C., Barth, G.A., Buhl, P., Detrick, R.S., Orcutt, J. & Harding, A., 1988. Magma distribution across ridge-axis discontinuities on the East Pacific Rise from multichannel seismic images, *Nature,* **336,** 156–158.

Mutter, J.C., Carbotte, S.M., Nedimović, M.R., Canales, J.P. & Carton, H., 2009. Seismic imaging in three dimensions on the East Pacific Rise, *EOS, Trans. Am. geophys. Un.,* **90**(42), 374–375.

Mutter, J.C., Carton, H., Marjanović, M., Carbotte, S., Canales, J.P. & Nedimović, M.R., 2010. Eruption-related changes in magma chamber structure at 9°50′N on the EPR from coincident reflection images, 1985 and 2008, *EOS, Trans. Am. geophys. Un.,* Abstract OS24A-01.

Mutter, J., Carbotte, S., Canales, J.P., Nedimović, M. & Carton, H., 2014. Multi-channel seismic shot data from the East Pacific Rise 9 degrees North Spreading Center Segment acquired during R/V Marcus G. Langseth expedition MGL0812 (2008), Integrated Earth Data Applications (IEDA). Available at: http://doi.org/10.1594/IEDA/31465410.1093/gji/ggv251.html, last accessed 25 June 2015.

Nooner, S.L., Webb, S.C., Buck, W.R. & Cormier, M.H., 2014. Posteruption inflation of the East Pacific Rise at 9°50′ N, *Geochem. Geophys. Geosys.,* **15,** doi:10.1002/2014GC005389.

Orcutt, J., Kennett, B., Dorman, L. & Prothero, W., 1975. A low velocity zone underlying a fast-spreading rise crest, *Nature,* **256,** 475–476.

Pelletier, H., 2008. AVO crossplotting revisited: a practitioner's perspective, *CSEG Recorder,* Focus Article, pp. 40–46.

Qin, R. & Buck, W.R., 2008. Why meter-wide dikes at oceanic spreading centers?, *Earth planet. Sci. Lett.,* **265,** 466–474.

Resnick, J.R., 1993. Seismic data processing for AVO and AVA analysis, in *Offset Dependent Reflectivity—Theory and Practice of AVO Analysis,* pp. 175–189, eds Castagna, J.P. & Backus, M.M., Society of Exploration Geophysicists.

Richards, P.G. & Frasier, C.W., 1976. Scattering of elastic wave from depth-dependent inhomogeneities, *Geophysics,* **41,** 441–458.

Ross, C., 2000. Effective AVO crossplot modeling: a tutorial, *Geophysics,* **65**(3), 700–711.
Rubin, K.H., Macdougall, J.D. & Perfit, M.R., 1994. ^{201}Po-^{210}Pb dating of recent volcanic eruptions on the seafloor, *Nature,* **368,** 841–844.
Rubin, K.H. *et al.*, 2012. Volcanic eruptions in the deep sea, *Oceanography,* **25**(1), 142–157.
Sacchi, M.D. & Ulrych, T.J., 1995. High-resolution velocity gathers and offset space reconstruction, *Geophysics,* **60,** 1169–1177.
Scheirer, D.S., Shank, T.M. & Fornari, D.J., 2006. Temperature variations at diffuse and focused flow hydrothermal vent sites along the northern East Pacific Rise, *Geochem. Geophys. Geosyst.,* **7,** Q03002, doi:10.1029/2005GC001094.
Shang, Z., McDonald, J.A. & Gardner, G.H.F, 1993. Automated extraction of AVA Information in the presence of structure, in *Offset Dependent Reflectivity—Theory and Practice of AVO Analysis,* pp. 199–208, eds Castagna, J.P. & Backus, M.M., Society of Exploration Geophysicists.
Shank, T.M., Fornari, D.J., Von Damm, K.L., Lilley, M.D., Haymon, R.M. & Lutz, R.A., 1998. Temporal and spatial patterns of biological community development at nascent deep-sea hydrothermal vents along the East Pacific Rise, *Deep Sea Res. Part II,* **45,** 465–515.
Sheriff, R.E., 1975. Factors affecting seismic amplitudes, *Geophys. Prospect.,* **23**(1), 125–138.
Shuey, R.T., 1985. A simplification of the Zoeppritz equations, *Geophysics,* **50,** 609–614.
Singh, S.C., Kent, G.M., Collier, J.S., Harding, A.J. & Orcutt, J.A., 1998. Melt to mush variations in crustal magma properties along the ridge crest at the southern East Pacific Rise, *Nature,* **394,** 874–878.
Singh, S.C., Collier, J.S., Harding, A.J., Kent, G.M. & Orcutt, J.A., 1999. Seismic evidence for a hydrothermal layer above the solid roof of the axial magma chamber at the southern East Pacific Rise, *Geology,* **27**(3), 219–222.
Singh, S.C. *et al.*, 2006. Seismic reflection images of the Moho underlying melt sills at the East Pacific Rise, *Nature,* **442**, 287–290.
Sinton, J.M. & Detrick, R.S., 1992. Mid-ocean ridge magma chambers, *J. geophys. Res.,* **97**(B1), 197–216.
Sohn, R.A., Fornari, D.J., Von Damm, K.L., Hildebrand, J.A. & Webb, S.C., 1998. Seismic and hydrothermal evidence for a cracking event on the East Pacific Risecrest at 9°50′N, *Nature,* **396,** 159–161.
Sohn, R.A., Hildebrand, J.A. & Webb, S.C., 1999. A microearthquake survey of the hightemperature vent fields on the volcanically active East Pacific Rise (9°50′N), *J. geophys. Res.,* **104,** 25 367–25 377.
Soule, S.A., Fornari, D.J., Perfit, M.R., Tivey, M.A., Ridley, W.I. & Schouten, H., 2005. Channelized lava flows at the East Pacific Rise crest 9°–10°N: the importance of off-axis lava transport in developing the architecture of young oceanic crust, *Geochem. Geophys. Geosyst.,* **6,** Q08005, doi:10.1029/2005GC000912.
Soule, SA., Fornari, D.J., Perfit, M.R. & Rubin, K., 2007. New insights into mid-ocean ridge volcanic processes from the 2005–2006 eruption of the East Pacific Rise, 9°46′N–9°56′N, *Geology,* **35**(12), 1079–1082.
Tolstoy, M. *et al.*, 2006. A sea-floor spreading event captured by seismometers, *Science,* **314,** 1920–1922.
Tolstoy, M., Waldhauser, F., Bohnenstiehl, D.R., Weekly, R.T. & Kim, W.-Y., 2008. Seismic identification of along-axis hydrothermal flow on the East Pacific Rise, *Nature,* **415,** 181–184.
Toomey, D.R., Purdy, G.M., Solomon, S.C. & Wilcock, W.S.D., 1990. The three-dimensional seismic velocity structure of the East Pacific Rise near latitude 9°30′N, *Nature,* **347,** 639–645.
Toomey, D.R., Jousselin, D., Dunn, R.A., Wilcock, W.S.D. & Detrick, R.S., 2007. Skew of mantle upwelling beneath the East Pacific Rise governs segmentation, *Nature,* **446,** 409–414.
Vera, E.E., Mutter, J.C., Buhl, P., Orcutt, J.A., Harding, A.J., Kappus, M.E., Detrick, R.S. & Brocher, T.M., 1990. The structure of 0- to 0.2-m.y.-old oceanic crust at 9°N on the East Pacific Rise from expanded spread profiles, *J. geophys. Res.,* **95**(B10), 15 529–15 556.
Von Damm, K., 2006. RESET06 - AT15–6 a response cruise to a volcanic eruption at the Ridge2000 East Pacific Rise integrated study site, Cruise Report, Available at: http://www.marine-geo.org/link/data/field/Atlantis/AT15-06/docs/AT15-06_CRUISE_REPORT_RESET06.pdf, last accessed 25 June 2015.
Von Damm, K.L., 1995. Controls on the chemistry and temporal variability of seafloor hydrothermal fluids, in *Seafloor Hydrothermal Systems: Physical, Chemical, Biologic and Geologic Interactions,* Vol. 91, pp. 222–248, eds Humphris, S.E., Zierenberg, R.A., Mullineaux, L.S. & Thompson, R.E., Geophysical Monograph Series, American Geophysical Union.
Von Damm, K.L., 2000. Chemistry of hydrothermal vent fluids from 9°–10° N, East Pacific Rise: "Time zero," the immediate posteruptive period, *J. Geophys. Res.,* **105,** 11 203–11 222.
Von Damm, K.L., 2004. Evolution of the hydrothermal system at East Pacific Rise 9°50′N: geochemical evidence for changes in the upper oceanic crust, in *Hydrothermal Interactions between the Lithosphere and Oceans,* Vol. 148, pp. 285–305, eds German, C.R., Lin, J. & Parson, L.M., Geophysical Monograph Series, American Geophysical Union.
Walden, A.T., 1991. Making AVO sections more robust, *Geophys. Prospect.,* **39,** 915–942.
Wanless, V.D. & Shaw, A.M., 2012. Lower crustal crystallization and melt evolution at mid-ocean ridges, *Nature Geosci.,* **5,** 651–655.
White, S.M., Haymon, R.M. & Carbotte, S., 2006. A new view of ridge segmentation and near-axis volcanism at the East Pacific Rise, 8–12°N, from EM300 multibeam bathymetry, *Geochem. Geophys. Geosyst.,* **7,** Q12O05, doi:10.1029/2006GC001407.
Widess, M.B., 1973. How thin is a thin bed?, *Geophysics,* **38,** 1176–1180.
Wilcock, W.S.D., Hooft, E.E.E., Toomey, D.R., McGill, P.R., Barclay, A.H., Stakes, D.S. & Ramirez, T.M., 2009. The role of magma injection in localizing black-smoker activity, *Nature Geosci.,* **2,** 509–513.
Xu, M., Canales, J.P., Carbotte, S.M., Carton, H., Nedimović, M.R. & Mutter, J.C., 2014. Variations in axial magma lens properties along the East Pacific Rise (9°30′–10°00′N) from swath 3D seismic imaging and 1D waveform inversion, *J. geophys. Res.,* **119,** doi:10.1002/2013JB010730.
Yilmaz, Ö., 2001. *Seismic data analysis, Processing, Inversion, and Interpretation of Seismic Data,* Society of Exploration Geophysicists.
Zha, Y., Webb, S.C., Nooner, S.L. & Crawford, W.C., 2014. Spatial distribution and temporal evolution of crustal melt distribution beneath the East Pacific Rise at 9°–10°N inferred from 3-D seafloor compliance modeling, *J. geophys. Res. Solid Earth,* **119,** doi:10.1002/2014JB011131.
Zoeppritz, K., 1919. Erdbebenwellen VIIIB, On the reflection and propagation of seismic waves, *Gottinger Nachrichten,* **I,** 66–84.

APPENDIX A

Bortfeld (1961) was the first to give linearizing approximation for the *P*-wave reflection coefficient derived by Zoeppritz (1919). Richards & Frasier (1976) and Aki & Richards (1980) assumed small changes in elastic parameters across the interface and grouped the terms as functions of density, V_p and V_s, respectively. Standard AVA analysis seeks to match observed amplitudes in velocity-corrected gathers to the theoretical amplitude curves obtained from Aki and Richards' approximation (e.g. Carazzone & Srnka 1993; Demirbag *et al.* 1993). However, this curve-fitting process has proved challenging (Foster, private communication, 2011), and significant efforts conducted in the past two decades have aimed to design techniques to facilitate AVA analysis.

When the terms are grouped as a function of the angle of incidence θ (Shuey 1985), the *P*-wave reflection coefficient can be written as:

$$R_{pp}(\theta) = A + B\sin^2\theta + C(\tan^2\theta - \sin^2\theta). \quad \text{(A1)}$$

Here, the angle of incidence θ is used as an approximation for the average of the incident θ_1 and transmitted θ_2, that is $\theta = (\theta_1 + \theta_2)/2$; the first term A is the vertical incidence reflection coefficient, the second term B contributes primarily at near- to mid-angles and the third term C dominates at far-angles. For small elastic

Table B1. Available volume calculations under the assumptions outlined in Appendix B. Note that in the calculations of the available AML volume only yellow (partially molten) and orange (mostly molten) regions are included.

Region 9°47.9′–9°52′N (7563 m)	× 10^6 m^3
V (volume of lava erupted)	18.2
D (volume of dykes = 1500 m × 1 m × 7563 m)	11.3
AML volume (only orange and yellow regions are taken into account)	
Y (yellow regions = 24 m × 700 m × 2000 m)	50.4
O (orange regions = 24 m × 700 m × 1312.5 m)	22.05
80 per cent AML volume	
Y_e = 80 per cent Y (AML in yellow region)	40.3
O_e = 80 per cent O (AML in orange region)	17.6
Mobilized magma volume	
Y_m = 50 per cent Y_e (30 per cent left in AML yellow region)	20.2
O_m = 25 per cent O_e (55 per cent left in AML orange region)	4.4
M (total mobilized volume = $Y_m + O_m$)	24.6
S (available magma volume to be emplaced onto the seafloor = M−D)	13.3

perturbations:

$$A = \frac{1}{2}\left(\frac{\Delta V_p}{\langle V_p\rangle} + \frac{\Delta\rho}{\langle\rho\rangle}\right),$$

$$B = \frac{1}{2}\frac{\Delta V_p}{\langle V_p\rangle} - 4\frac{V_s^2}{\langle V_p\rangle^2}\frac{\Delta V_s}{\langle V_s\rangle} - 2\frac{V_s^2}{\langle V_p\rangle^2}\frac{\Delta\rho}{\langle\rho\rangle} \quad \text{and}$$

$$C = \frac{1}{2}\frac{\Delta V_p}{\langle V_p\rangle}$$

where V_{p2}, V_{p1}, V_{s2}, V_{s1}, ρ_2 and ρ_1 are *P*-wave velocities, *S*-wave velocities and densities below and above the interface, respectively, and $\Delta V_p = V_{p2} - V_{p1}$; $\langle V_p\rangle = (V_{p2} + V_{p1})/2$; $\Delta V_s = V_{s2} - V_{s1}$ $\langle V_s\rangle = (V_{s2} + V_{s1})/2$; $\Delta\rho = \rho_2 - \rho_1$ $\langle\rho\rangle = (\rho_2 + \rho_1)/2$.

For relatively small angles (i.e. less than 30°) the third term can be neglected (Shuey 1985) and the *P*-wave reflection coefficient can be approximated by:

$$R_{pp}(\theta) = A + B\sin^2\theta. \qquad \text{(A2)}$$

In this two-term approximation, known also as Shuey's approximation, varies linearly with respect to angle of incidence and the relationship is described by two seismic attributes: *A*—intercept and *B*—slope or gradient.

APPENDIX B

The lava flow mapped by Soule *et al.* (2007) and Fundis *et al.* (2010) extends between ∼9°45.6 and 55.7′N, that is, 18.5 km. Assuming an average depth of the AML of 1.5 km and a uniform dyke width of 1 m (e.g. Qin & Buck 2008; note that this might be an underestimate, as 13 yr of seafloor spreading between 1992 and 2005 would amount to ∼1.43 m of opening), the volume of melt intruded as a feeder dyke beneath the seafloor extent of the lava flow is 27.8 × 10^6 m^3. The estimate of the total volume of the flow is 22 × 10^6 m^3 (Soule *et al.* 2007) revised to ∼24 × 10^6 m^3 on the basis of the mapping of Fundis *et al.* (2010).

In the following calculations, we assume that only the portions of the AML characterized as partially molten and mostly molten contributed melt during the eruption. We assign melt fractions of 30 per cent to the partially molten portion (consistent with <40 per cent obtained by Xu *et al.* 2014 at 9°49.1′N), 80 per cent to the highly molten portions (consistent with >70 per cent obtained by Xu *et al.* 2014 at 9°42.8′N), and 55 per cent to the mostly molten portions (as the intermediate value between the above two). We assume the AML has a constant thickness of 24 m (in keeping with the results of Xu *et al.* 2014) and a constant width of 700 m. A model of subvertical magma ascent is considered, in which each AML segment contributes to the lava flow erupted above it (e.g. Carbotte *et al.* 2013).

Between 9°47.9 and 52′N, 75 per cent of the total flow volume was erupted, that is 18.2 × 10^6 m^3; this is where the most voluminous flow lobes, highest inferred effusion rates (Soule *et al.* 2007; Fundis *et al.* 2010) and highest inferred AML temperature (Goss *et al.* 2010) are encountered (Fig. 10b). Assuming the pre-eruption melt fraction was 80 per cent within this region, dropping to 30 per cent for the AML sections characterized as partially molten post-eruption and 55 per cent for the sections characterized as mostly molten (leaving the highly molten sections unchanged), the AML alone would have contributed a volume of 13.3 × 10^6 m^3 of lavas between 9°47.9 and 52′N in addition to the coincident intruded volume of 11.3 × 10^6 m^3 (Table B1). This contribution is thus insufficient to explain the estimate of 18.2 × 10^6 m^3 erupted within this region. By contrast, south of 9°47.9′N and north of 9°52′N, the extruded volume is about 25 per cent of the total flow volume and there is no deficit of available melt within the AML prior to the eruption.